



Tribology of HVOF- and HVAF-sprayed WC–10Co4Cr hardmetal coatings: A comparative assessment



G. Bolelli ^{a,*}, L.-M. Berger ^{b,1}, T. Börner ^{a,b,2}, H. Koivuluoto ^c, L. Lusvarghi ^a, C. Lyphout ^d, N. Markocsan ^d, V. Matikainen ^c, P. Nylén ^d, P. Sassatelli ^a, R. Trache ^b, P. Vuoristo ^c

^a Dipartimento di Ingegneria “Enzo Ferrari”, University of Modena and Reggio Emilia, Via Pietro Vivarelli 10/1, I-41125 Modena (MO), Italy

^b Fraunhofer-Institut für Werkstoff- und Strahltechnik (IWS), Winterbergstr. 28, D-01277 Dresden, Germany

^c Department of Materials Science, Tampere University of Technology, Korkeakoulunkatu 6, FI-33720 Tampere, Finland

^d Department of Engineering Science, University West, Gustava Melins gata 2, SE-461 86 Trollhättan, Sweden

ARTICLE INFO

Article history:

Received 10 September 2014

Accepted in revised form 20 January 2015

Available online 28 January 2015

Keywords:

Hardmetal

WC–10Co4Cr

High velocity oxy-fuel (HVOF)

High velocity air-fuel (HVAF)

Sliding wear

Abrasive wear

ABSTRACT

This paper provides a comprehensive assessment of the sliding and abrasive wear behaviour of WC–10Co4Cr hardmetal coatings, representative of the existing state-of-the-art. A commercial feedstock powder with two different particle size distributions was sprayed onto carbon steel substrates using two HVOF and two HVAF spray processes.

Mild wear rates of $<10^{-7}$ mm³/(Nm) and friction coefficients of ≈ 0.5 were obtained for all samples in ball-on-disk sliding wear tests at room temperature against Al₂O₃ counterparts. WC–10Co4Cr coatings definitely outperform a reference electrolytic hard chromium coating under these test conditions. Their wear mechanisms include extrusion and removal of the binder matrix, with the formation of a wavy surface morphology, and brittle cracking. The balance of such phenomena is closely related to intra-lamellar features, and rather independent of those properties (e.g. indentation fracture toughness, elastic modulus) which mainly reflect large-scale inter-lamellar cohesion, as quantitatively confirmed by a principal component analysis. Intra-lamellar dissolution of WC into the matrix indeed increases the incidence of brittle cracking, resulting in slightly higher wear rates. At 400 °C, some of the hardmetal coatings fail because of the superposition between tensile residual stresses and thermal expansion mismatch stresses (due to the difference between the thermal expansion coefficients of the steel substrate and of the hardmetal coating). Those which do not fail, on account of lower residual stresses, exhibit higher wear rates than at room temperature, due to oxidation of the WC grains.

The resistance of the coatings against abrasive wear, assessed by dry sand–rubber wheel testing, is related to inter-lamellar cohesion, as proven by a principal component analysis of the collected dataset. Therefore, coatings deposited from coarse feedstock powders suffer higher wear loss than those obtained from fine powders, as brittle inter-lamellar detachment is caused by their weaker interparticle cohesion, witnessed by their systematically lower fracture toughness as well.

© 2015 Elsevier B.V. All rights reserved.

1. Introduction

Hardmetal coatings deposited by the high velocity oxy-fuel (HVOF) spray process exhibit high density and mechanical strength. This results from the high momentum of the feedstock powder particles at the moment of impact on the substrate [1] and from their significantly lower temperature, much more suitable to hardmetal compositions than that attained e.g. in atmospheric plasma spraying (APS) processes. These coatings accordingly find a large variety of industrial applications

for the protection of mechanical components against sliding and abrasive wear at various temperatures [2] and in different environments. They are also listed among the most promising alternatives to hard chromium electroplating [3], due to their technical advantages [3,4] coupled to the lower environmental and lifecycle impact of the deposition process [5]. This is of particular interest as the chromium electroplating technique is facing regulatory restrictions due to its environmental and health hazardousness [6,7].

The properties of thermal spray hardmetal coatings, including their wear resistance in different tribological conditions, may however vary as a function of the feedstock powder properties, the spray process, and the deposition parameters, as shown e.g. by a number of studies on WC-based materials [8–12]. From these studies, it is inferred that some of the most influential factors include the selection of the HVOF spray process (among the many commercially available ones) [1,

* Corresponding author. Tel.: +39 059 2056233; fax: +39 059 2056243.

E-mail address: giovanni.bolelli@unimore.it (G. Bolelli).

¹ Present address: Fraunhofer-Institut für Keramische Technologien und Systeme (IKTS), Germany.

² Present address: Institut für Korrosionsschutz Dresden GmbH, Germany.

8–11], the process parameters [10,13], the properties of the carbide (WC- or Cr₃C₂-based) and the binder phase, as well as the composition and the properties of the feedstock powder (size of particles [13–15] and of carbide grains [16–18]). Specifically, the need to heat powder particles enough to achieve plastic deformation of the feedstock powder particles at the moment of impact, and, consequently, good inter-lamellar bonding must be balanced with the contrasting need to prevent changes of the chemical and phase composition [19]. This means a certain degree of decarburisation is unavoidable when using the HVOF process.

In addition to the HVOF processes, the high velocity air-fuel (HVOF) process was developed nearly in the same period of time [20]. Due to low deposition efficiencies of the first generations of spray guns, this process did not find wide distribution in the industry. Significant constructive enhancements about 15 years ago increased the economic effectiveness. Together with lower thermal load and the higher velocities of the feedstock powder particles, this spray process represents an alternative to the HVOF spray processes. This broadens the range of available choices by offering the possibility to deposit dense coatings with excellent mechanical properties and high wear resistance [19].

Nowadays, the composition WC–10 wt.% Co–4 wt.% Cr (designated as WC–10Co4Cr in the following) is one of the most important commercially available ones and widely used for the preparation of coatings having simultaneously high wear and corrosion resistance [12]. Intensive studies on this composition have started at the end of 1990-ies only [21] and were closely connected with the increasing use of HVOF-sprayed coatings [12]. The ratio of cobalt to chromium in this composition is 2:1 by volume and the nominal content of carbon is 5.27% [22]. WC, the η -phase (Co,Cr)₃W₃C, and a (Co,Cr,W) alloy binder are expected to be in thermodynamic equilibrium. However, in the case of higher carbon content, in equilibrium conditions a (Co,Cr,W)₇C₃ phase will appear instead of the η -phase [22,23]. In all cases, chromium is contained both in the metallic binder and the hard phase [22–24]. Another important feature of chromium addition is a significant melting point reduction compared to plain WC–Co [23]. In general, it seems that WC–10Co4Cr is a good empirically derived and balanced formulation for the preparation of simultaneous wear and corrosion resistant coatings [22].

Under sliding and abrasive wear conditions, properly manufactured WC-based hardmetal coatings exhibit matrix abrasion, until unsupported WC grains are fractured and/or pulled out of the surface [25,26]. Micro-scale plastic deformation of the top surface has also been noted after sliding wear testing in some studies [27–29]. In case of excessive changes of phase composition, the coatings reportedly become very brittle, with surface and sub-surface crack propagation dominating their tribological behaviour in sliding and abrasive conditions [11, 16–18,30,31]. When particles are scarcely heated during spraying, by contrast, inter-lamellar detachment is likely to occur [31].

Many of the cited papers, however, consider a limited set of coatings, which do not allow a comprehensive assessment of different technologies and different feedstock powders. Even those which report about systematic studies, such as the literature on the comparison between HVOF- and HVOF-sprayed WC-based hardmetal coatings [11,32–34], have limitations, such as the description of samples not belonging to the state-of-the-art due to the use of older deposition technologies and/or of non-optimal parameters, or the lack of a detailed investigation of wear mechanisms. Little information is also available on the high-temperature wear behaviour of WC-based hardmetal coatings (few examples are given in [28,29,35,36]).

The present research therefore aims to provide a comprehensive assessment of the tribological properties of HVOF- and HVOF-sprayed WC–10Co4Cr hardmetal coatings obtained by the use of feedstock powders with different particle size distributions. These coatings provide a representative picture of the state-of-the-art. Focus is made on the characterisation of the wear behaviour under dry sliding wear (at room temperature and at 400 °C) and abrasive wear conditions.

2. Experimental

2.1. Sample manufacturing

One commercial powder composition (WC–10Co4Cr), with two different particle size distributions suitable for the HVOF and HVOF spray processes, was provided by one manufacturer and sprayed using four different thermal spray techniques: a liquid-fuelled (paraffine) JP-5000 HVOF spray process (Praxair-TAFA, Concord, NH, USA), a gas-fuelled (propane) Diamond Jet 2700 HVOF spray process (Sulzer-Metco, Wohlen, Switzerland), and the M2 and M3 HVOF spray processes (Unicoat Technologies Inc., Oilville VA, USA). The latter differ both in torch construction and in the employed fuels, respectively methane and propane. A summary of all powders, processes and coatings employed in this study, together with their conventional designations used hereafter, is provided in Table 1.

All coatings were sprayed onto 100 × 50 × 8 mm plates of low-carbon Domex 355 steel (chemical composition, in weight %: C < 0.10, Mn = 1.50, P < 0.025, S < 0.010, Fe = balance), which were grit-blasted before deposition. The samples were mounted on a rotating sample holder; the resulting coatings had a thickness of ≈ 250–300 μm. Process parameters for all deposition techniques had previously been optimised in order to obtain dense coatings with high deposition efficiency.

As a term of comparison, two electroplated hard chromium layers (both ≈ 300 μm thick) were deposited at an industrial facility onto the same plates (subjected to a preliminary grinding process according to the manufacturer's standard procedures), using a conventional CrO₃ + H₂SO₄ Fink's electroplating bath with proprietary additives.

2.2. Microstructural characterisation

The cross-sectional microstructure of the coatings and of the feedstock powders was characterised by scanning electron microscopy (SEM: Philips XL30 and Quanta-200, FEI, Eindhoven, NL) equipped with energy-dispersive X-ray (EDX) microanalysis (DX-4 EDAX, USA and Inca, Oxford Instruments Analytical, Abingdon, UK). Both the powders and the coated samples were cold-mounted in epoxy resin, ground with diamond papers (up to 1200 mesh) and polished with diamond slurries (6 μm and 3 μm) and colloidal silica suspension.

Image analysis was performed on SEM micrographs of the coating cross-sections, obtained using a TM3000-Tabletop Microscope (HITACHI), in order to determine the volume fraction of pores and of carbide grains and the size of the latter in each sample. A specially developed image thresholding algorithm utilising the Aphelion® image analysis software was applied on 20 SEM pictures (7000× magnification) per sample.

The phase composition of the feedstock powders and of all coatings was assessed by X-ray diffraction (XRD: Empyrean, PANalytical, Almelo, NL), performed with Cu-Kα radiation in the 20° ≤ 2θ ≤ 120° range. The integral intensities of the (100) peak of WC (*I*_{WC}) and of the (101) peak of W₂C (*I*_{W₂C}) were assessed by pattern fitting using pseudo-Voigt functions and the index of carbide retention (*I*), quantifying the retention of the WC phase against the formation of W₂C, was computed as $I = I_{WC} / (I_{WC} + I_{W_2C})$, according to the definition in [10].

In addition, both fractions of the feedstock powder were analysed for their total carbon content by the combustion method (WC 600, LECO Corporation, St. Joseph, MI, USA) and for their magnetic saturation (Sigmameter, Setaram, Saint-Cloud, France). The latter method allows to obtain fast additional information about the state of cobalt in the hardmetal composition, in combination with XRD results, and it is described in more detail elsewhere [22].

The microhardness of the coatings was measured on polished cross-sections by Vickers indentation according to the standard ASTM E-384-10. Measurements were carried out using a Vickers indenter (Shimadzu Microhardness Tester) at three different loads of 100 gf (≈ 1 N), 300 gf (≈ 3 N) and 500 gf (≈ 5 N), with a dwell time of 15 s. For each load, 20

Table 1

List of powders, deposition techniques and resulting coatings used in this study, together with their conventional designations.

Powder material				Deposition process (designation)			
Composition (wt.%)	Commercial designation	Size (μm)	Ref. code	HVAF M3 ^{a)} (P1)	HVOF JP5000 ^{b)} (P2)	HVOF DJ2700 ^{c)} (P3)	HVAF M2 ^{d)} (P4)
WC–Co–Cr 86–10–4	AMPERIT® ^{e)} 558.059	– 30 + 5	W1	P1W1	P2W1	P3W1	P4W1
	AMPERIT® ^{e)} 558.074	– 45 + 15	W2	P1W2	P2W2	P3W2	P4W2

^{a)} M3-HVAF torch, Uniquocoat, Oilville, Virginia, USA.

^{b)} JP5000 torch, Praxair-Tafa, Concord, NH, USA.

^{c)} Diamond Jet 2700, Sulzer-Metco, Wohlen, Switzerland.

^{d)} M2-HVAF torch, Uniquocoat, Oilville, Virginia, USA.

^{e)} H.C. Starck GmbH, Laufenburg, Germany.

impressions, evenly distributed in a half circle through the entire test panel, were made on each coating cross-section.

Indentation fracture toughness (IFT) was also assessed by performing indentations into the polished cross-sections of the coatings using a Vickers-shaped indenter (12 indents, Mitutoyo AVK C1). A high peak load of 5 kgf (≈ 49 N, load period 10 s) was employed in order to induce crack propagation from the indent corners. Fracture toughness was determined by measuring crack lengths on optical micrographs ($200\times$ magnification, 2560×1920 pixel resolution) using ImageJ [37]. Only cracks parallel to the substrate starting at the left and right tip of indents, respectively, were considered (Fig. 1), according to the method described in [38]. The critical stress intensity (K_{IC}) was calculated according to Niihara et al. [39] based on the Palmqvist crack model.

The Young's modulus has been measured with the surface acoustic wave method (LAwave®), the details of sample preparation and measurement technique are given elsewhere [40,41].

In order to determine the thermal expansion coefficient of the WC–10Co4Cr coating and of the steel substrate, optical dilatometer measurements (Horizontal Optical Dilatometer Misura® ODLT, Expert System Solutions, Modena, Italy) were performed on $50 \times 5 \times 0.3$ mm specimens obtained from sample P2W1 by metallographic cutting and grinding with SiC papers. Measurements were carried out in air at a heating rate of 5 °C/min up to 400 °C. Two heating cycles were performed and the thermal expansion coefficient values were obtained from the second cycle, in order to avoid artefacts due e.g. to the release of residual stresses, in accordance with the procedure described in [42].

2.3. Wear testing

Rotating ball-on-disk tests (High-Temperature Tribometer, CSM Instruments, Peseux, Switzerland) were performed according to

the ASTM G99 standard on ground and polished coating surfaces ($R_a \approx 0.02$ μm). The stationary counterparts were sintered Al_2O_3 spheres (nominal hardness $\text{HV} \approx 1900$) of 6 mm diameter. Test conditions include normal load of 10 N, relative sliding speed of 0.10 m/s, wear track radius of 7 mm and an overall sliding distance of 5000 m. Tests were performed both at room temperature (temperature ≈ 25 °C, relative humidity $\approx 60\%$) and at 400 °C. In the latter case, the samples were induction heated from the base plate of the tribometer and their temperature was monitored by a thermocouple in contact with their rear surface. The samples were heated for 1 h up to 400 °C and they were allowed for additional 30 min to stabilise in isothermal conditions. At least two tests were performed for each coating.

The friction coefficient was monitored during the test using a load cell attached to the ball holding arm. The volume losses of samples and counterparts were assessed by optical confocal profilometry (Conscan profilometer, CSM Instruments) of wear tracks and by optical microscopy measurement of worn cap diameters, respectively. Data were normalised over sliding distance and normal load in order to obtain the wear rates.

Moreover, the morphology of the wear scars on the samples was studied by SEM. The phase composition of the debris clusters attached to the wear scar and of the loose debris particles laying outside the wear scar was assessed by micro-Raman spectroscopy (LabRam, Horiba Jobin-Yvon, Villeneuve d'Ascq, France) using a 632.81 nm-wavelength He:Ne laser radiation focused through $50\times$ and $100\times$ objectives. Some representative samples of loose debris particles were also collected on a Cu grid for observation by transmission electron microscope (TEM: JEM 2010, Jeol, Tokyo, Japan), equipped with EDX microanalysis detector (INCA).

Abrasion wear behaviour of the coatings was evaluated using a modified version of the ASTM G65 dry sand–rubber-wheel (DSRW)

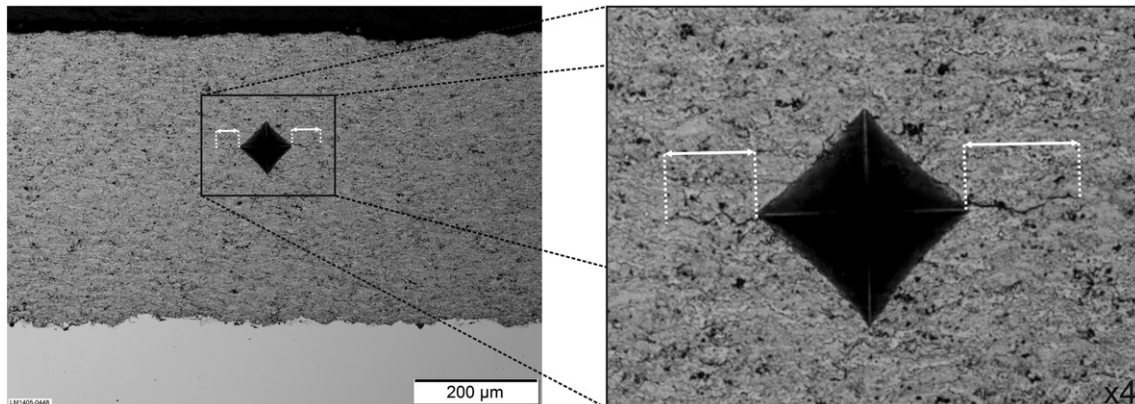


Fig. 1. Optical micrograph of a cracked Vickers indentation employed for fracture toughness measurement, with indication of horizontal crack lengths.

abrasion wear test, where five samples were tested simultaneously. Blocky-shaped dry quartz sand (SiO_2) with a grain size ranging from 0.1 to 0.6 mm was used as the abrasive. The flow rate of the abrasive was 25 g/min. Sample surfaces were ground using 1200 grit SiC paper ($R_a \approx 8 \mu\text{m}$) before testing. During the test, the samples were pressed with a normal load of 23 N against a rotating rubber wheel with a surface speed of 1.64 m/s. The test lasted for 60 min for an overall wear distance of 5904 m. The samples were weighed every 12 min using an analytical scale with 0.001 g accuracy, in order to determine their mass loss, which was converted to volume loss using density values. Specifically, the density of each hardmetal coating was computed based on its volume fraction of pores and carbide grains determined by image analysis (Section 2.2), using $\rho_{\text{WC}} = 15.7 \text{ g/cm}^3$ as the density of WC and $\rho_{\text{binder}} = 8.6 \text{ g/cm}^3$ [43] as the density of the binder matrix (in the absence of precise data, the latter value was assumed to be approximately equal to that of a Stellite® alloy). Some of the coatings contained significant amounts of W_2C , which has a higher density (17.2 g/cm^3) than WC. However, the error for the conversion into volume loss made by neglecting these amounts of W_2C has been estimated to be smaller than the error of the measurement. The density of electrolytic hard chromium was assumed to be $\rho_{\text{EHC}} = 7.2 \text{ g/cm}^3$ [44].

Worn surfaces were also observed by SEM (XL40, FEI).

2.4. Residual stress measurements

Residual stresses were measured by X-ray diffraction (X'Pert PRO diffractometer, PANalytical, Almelo, NL: Cu-K α radiation) on as-deposited samples P1W1, P2W1, P3W1 and P4W1 (Table 1).

Measurements were performed according to the $\sin^2\psi$ method in ω -tilt configuration. A line focus source with parallel beam set-up, comprising an X-ray mirror on the incident beam path and a gas-proportional detector with parallel plate collimator on the diffracted beam path, was employed in order to minimise errors due to sample positioning in the vertical direction [45,46].

The (211) peak of WC, located at $2\theta \approx 117.3^\circ$, was acquired with a 2θ scan range of 4° . Measurements were performed at symmetric positive as well as pseudo-negative ψ angles corresponding to $\sin^2\psi$ values of 0, 0.1, ..., 0.4, and they were repeated at three different sample orientation angles (φ) of 0° , 45° and 90° , where $\varphi = 0^\circ$ and $\varphi = 90^\circ$ correspond to the directions parallel to the major and minor side of the rectangular samples, respectively. The interplanar spacing $d_{\varphi,\psi}^{(211)}$ was therefore obtained at each ψ, φ position and the corresponding lattice strain was computed as $\varepsilon_{\varphi,\psi}^{(211)} = (d_{\varphi,\psi}^{(211)} - d_0^{(211)})/d_0^{(211)}$, where $d_0^{(211)}$ is the unstressed interplanar spacing. According to [47], assuming a plane stress condition, the $\sin^2\psi$ equation can be written for the three φ orientations to yield the following relations (1.1 to 1.3):

$$\varepsilon_{0^\circ,\psi}^{(211)} = \frac{1}{2}S_2^{(211)}\sigma_{11}\sin^2\psi + S_1^{(211)}(\sigma_{11} + \sigma_{22}) \quad (1.1)$$

$$\varepsilon_{90^\circ,\psi}^{(211)} = \frac{1}{2}S_2^{(211)}\sigma_{22}\sin^2\psi + S_1^{(211)}(\sigma_{11} + \sigma_{22}) \quad (1.2)$$

$$\varepsilon_{45^\circ,\psi}^{(211)} = \frac{1}{2}S_2^{(211)}\left(\frac{\sigma_{11} + \sigma_{22}}{2} + \tau_{12}\right)\sin^2\psi + S_1^{(211)}(\sigma_{11} + \sigma_{22}) \quad (1.3)$$

The normal stress components σ_{11} and σ_{22} are therefore obtained from the slopes of the linear plots of $\varepsilon_{\varphi,\psi}^{(211)}$ vs. $\sin^2\psi$ for $\varphi = 0^\circ$ and $\varphi = 90^\circ$, respectively (Eqs. (1.1) and (1.2)). Using these values together with the slope of the plot for $\varphi = 45^\circ$, the in-plane shear stress component τ_{12} is then obtained according to Eq. (1.3).

The elastic constants of WC along the (211) direction are $\frac{1}{2}S_2^{(211)} = 2.44 \times 10^{-6} \text{ MPa}^{-1}$ and $S_1^{(211)} = -4.10 \times 10^{-7} \text{ MPa}^{-1}$, respectively [48].

The unstressed lattice spacing $d_0^{(211)}$ is not known a priori: it is possible to replace its value by the interplanar spacing measured at $\psi = 0^\circ$,

i.e. assuming $d_0^{(211)} \approx d_{\varphi,\psi=0^\circ}^{(211)}$, with a limited error (not greater than 1% [49]). The result, however, is further refined by an iterative procedure. By setting $\psi = 0^\circ$ in Eqs. (1.1) to (1.3), it follows:

$$\begin{aligned} \frac{d_{\varphi,\psi=0^\circ}^{(211)} - d_0^{(211)}}{d_0^{(211)}} &= \varepsilon_{\varphi,\psi=0^\circ}^{(211)} = S_1^{(211)}(\sigma_{11} + \sigma_{22}) \rightarrow d_0^{(211)} \\ &= \frac{d_{\varphi,\psi=0^\circ}^{(211)}}{1 + S_1^{(211)}(\sigma_{11} + \sigma_{22})} \end{aligned} \quad (2)$$

The values of σ_{11} , σ_{22} and τ_{12} first obtained in the hypothesis that $d_0^{(211)} \approx d_{\varphi,\psi=0^\circ}^{(211)}$ are therefore adjusted by re-calculating $d_0^{(211)}$ with Eq. (2) until convergence is reached.

3. Results and discussion

3.1. Feedstock powder characterisation

The feedstock powders W1 and W2 appear very dense (Fig. 2A-D), with small WC grains, producing a bright contrast in those SEM micrographs, and some large dark grey areas. The diffraction peaks in XRD pattern of the feedstock powders, presented together with those of the coatings in Fig. 3, indicate the presence of at least one more phase, apart from WC and metallic f.c.c.-Co. In order to determine the composition of the dark grey areas which are probably associated with this phase, the result of the EDX microanalysis are displayed in Fig. 2E for the area marked in Fig. 2C. These dark areas, containing cobalt and chromium as main components together with very little tungsten, most probably correspond to a $(\text{Co,Cr,W})_7\text{C}_3$ carbide. According to a short summary of phase formation for the WC–10Co4Cr composition [22], above the solubility limit of chromium in the binder at high carbon content $(\text{Co,Cr,W})_7\text{C}_3$ carbides can be formed. The results of the experimental study of Zackrisson et al. [50] and a study on the effect of chromium on phase equilibria in WC–Co hardmetals by Frisk and Markström [23] have shown similar results. It should be mentioned that the $(\text{Co,Cr,W})_7\text{C}_3$ phase is difficult to distinguish from the f.c.c.-Co and from the η -phase (M_6C) in the X-ray diffraction pattern. The position of the two main diffraction peaks of Cr_7C_3 (respectively located at $2\theta = 44.2^\circ$ and $2\theta = 42.5^\circ$ according to the JCPDF 36-1482 file) are very close to those of f.c.c.-Co ($2\theta = 44.2^\circ$, JCPDF 15-806) and of the η -phase ($2\theta = 42.4^\circ$, JCPDF 27-1125), and some peak shift due to Co and W substituting for Cr in the M_7C_3 lattice may further enhance the overlapping. Such dark areas were found also in the cross-sections of other commercial agglomerated and sintered WC–10Co4Cr feedstock powders, published elsewhere [51–53].

The total carbon content was 5.45 wt.% and 5.44 wt.% for the W1 and W2 powders, respectively. Both values are significantly higher than the nominal content of 5.27 wt.% in the composition WC–10Co4Cr. This is an additional indication of the existence of $(\text{Co,Cr,W})_7\text{C}_3$ in the feedstock powder. All feedstock powders produced by sintering and crushing, studied earlier [22], had a total carbon content below the nominal carbon content, and thus contained the η -phase instead.

The magnetic saturation was $7.5 \mu\text{Tm}^3/\text{kg}$ and $8.1 \mu\text{Tm}^3/\text{kg}$ for the W1 and W2 powders, respectively. These values are of the same order of magnitude as those measured on sintered and crushed feedstock powders with a carbon content below the nominal one [22]. When the carbon content is above the nominal value, cobalt is largely contained in the $(\text{Co,Cr,W})_7\text{C}_3$ phase as discussed previously, whereas it enters the η -phase when the carbon content is below the nominal value: in both cases, therefore, only a limited amount of metallic cobalt is left in the matrix. In addition, the magnetic saturation of this metallic cobalt might be decreased by some dissolved chromium.

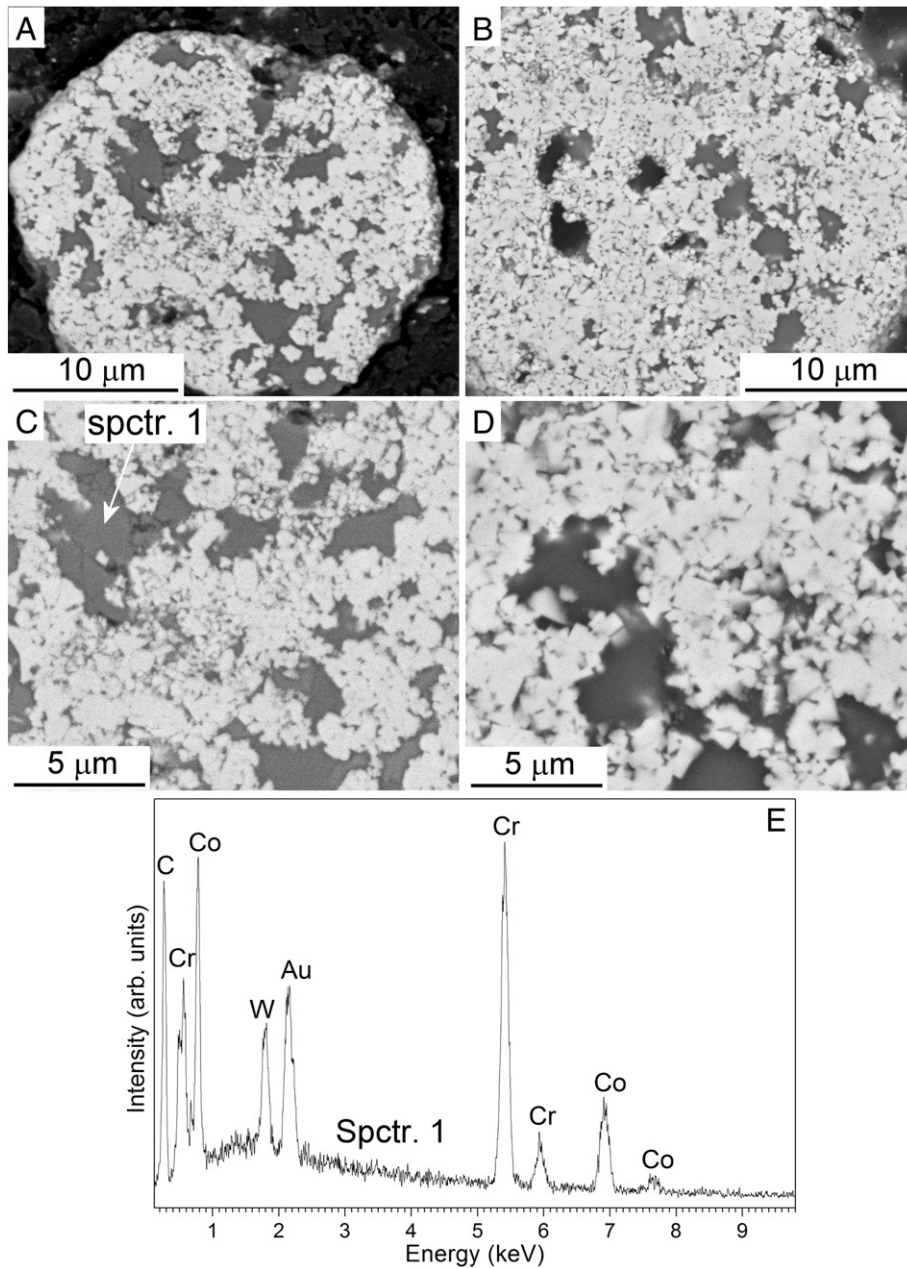


Fig. 2. SEM micrographs of the cross-section of the W1 (A,C) and W2 (B,D) feedstock powders, with EDX microanalysis (E) acquired on the area marked in panel C.

3.2. Coating microstructures

All coatings have thicknesses of 250–300 μm, as expected (Section 2.1). They exhibit macroscopically dense microstructures (Fig. 4A,C,E,G) with low porosity detectable at these magnifications. At greater magnifications, some pores (producing black contrast in backscattered electron imaging mode) become visible (Fig. 4B,D,F,H). Specifically, image analysis showed (Table 2) that the fine feedstock powder results in less porous coatings (W1-series) than the coarse one (W2-series), although the scatter of the experimental data is quite large.

In greater detail, the coatings deposited by the HVOF processes (P2- and P3-series: Fig. 4D,F) differ from those deposited by HVOF processes (P1- and P4-series: Fig. 4B,H). In the latter, due to the low HVOF process temperatures, the changes to the chemical and phase compositions were minimal or absent, also all of the WC grains contained in the

feedstock powders (Fig. 2A–D), including the finest (sub-micrometric) ones, are found in the coating (Fig. 4B,H) and they exhibit the same, angular morphology. In the HVOF-sprayed coatings, due to the higher process temperature a higher degree of melting and more intensive metallurgical reactions occur, accompanied with a more intense carbon loss. This leads to the disappearance of the dark grey $(\text{Co,Cr,W})_7\text{C}_3$ grains (Fig. 4D,F). Moreover, qualitative inspection of the SEM micrographs indicates that some of the finest carbide grains were partly lost and the remaining ones exhibit more rounded edges, as a consequence of decarburisation and/or of dissolution in the molten matrix (Fig. 4D,F). Accordingly, the matrix phase acquires a brighter backscattered electrons contrast level in splats where WC dissolution was more pronounced. The alteration of WC grains could however be restrained within acceptable levels in all cases: the differences between the average WC sizes in the various samples (as determined by image analysis, Section 2.2) are indeed smaller than the experimental uncertainty (Table 2).

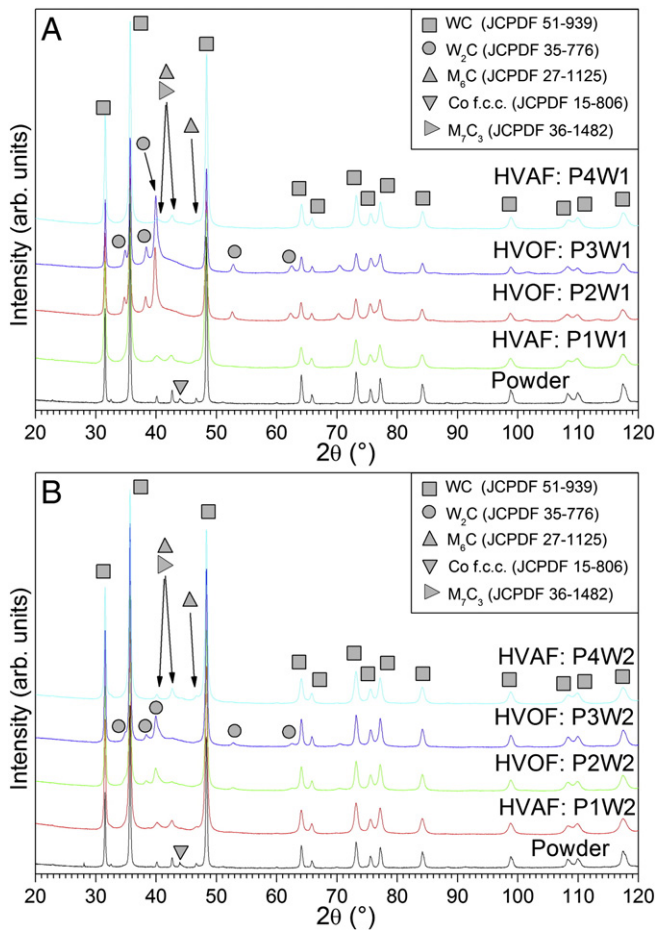


Fig. 3. XRD patterns of the W1 (A) and W2 (B) feedstock powders and of all corresponding WC–CoCr coatings.

The carbon loss of the HVOF-sprayed coatings (P2- and P3-series) is however perceivable through XRD patterns. The diffraction peaks of W_2C appear (Fig. 3) and, at the same time, peaks of $(Co,Cr,W)_7C_3$ existing in the feedstock powder, as discussed in Section 3.1, disappear. The main diffraction peak of W_2C , located at $2\theta \approx 39.94^\circ$, is slightly shifted from the theoretical position ($2\theta \approx 39.57^\circ$, as listed in the JCPDF 35-776 file): in accordance with [22,54], this means that the W_2C phase contains some Cr, formed as a result of metallurgical interactions during the spray process. Namely, a $(W,Cr)_2C$ composition is formed: from the peak positions and from the corresponding lattice parameters, the Cr content, extrapolated from the graph given in [54] according to the procedure previously outlined in [51], is approximately 9 mol%. This value is quite similar to the 6 mol% content reported for an analogous HVOF-sprayed WC–10Co4Cr coating [51].

The HVOF-sprayed coatings (P1- and P4-series), by contrast, contain no detectable W_2C and retain the same phase composition of the corresponding feedstock powders (Fig. 3), with peaks belonging to a f.c.c. Co-based solid solution and to the $(Co,Cr,W)_7C_3$ carbide.

Diffraction peaks, however, are broader in the patterns of the HVOF-sprayed coatings than in the patterns of the powders (Fig. 3), probably because of the extensive plastic deformation of the particles upon impact, so that the f.c.c.-Co phase peaks become nearly undetectable in the former.

Assuming the XRD technique has a detection threshold of about 2%, the index of WC retention is $\geq 98\%$ for all HVOF-sprayed coatings, whereas the values for the HVOF-sprayed coatings was between 54% and 84% (Table 2). Specifically, the coatings deposited using the finer feedstock powder (P2W1, P3W1) exhibit the lowest values of WC

retention. Finer powder particles are proposed to be more thoroughly heated in the flame.

3.3. Mechanical properties

Hardness (Fig. 5), indentation fracture toughness and elastic modulus (Fig. 6A,B) data highlight important trends. On the one hand, whilst the two HVOF processes produce similar results, the M3-HVOF process produces harder, tougher coatings with higher elastic modulus than the M2-HVOF process, which may be due to differences in torch architectures, in fuel gases and in other process conditions (Section 2.1).

Specifically, elastic modulus values have very low data scatter, as testified by the standard deviation plotted as error bar in Fig. 6B. The magnitude of the differences between the various samples can therefore be quantitatively evaluated by direct comparison of the average values. Indentation fracture toughness data is more scattered (Fig. 6A); therefore, in order to understand which samples have a statistically meaningful difference, the Student's *t*-test is needed. The average values of two data sets can be considered significantly different if the probability (*p*) that the means are identical (i.e. the probability of the "null hypothesis"), computed through a paired-sample Student's *t*-test or a two-sample *t*-test depending on whether the two data sets have different or identical variances (as determined through a preliminary *F*-test), is $p < 0.05$. The results, plotted in the table associated to Fig. 6A, confirm that, for most of the pairs of P1-series and P4-series samples, the differences between the average K_{IC} values are indeed significant. Similar considerations hold for Vickers microhardness; the overall *p*-values table can be found in the supplementary data provided with the paper.

On the other hand, for each deposition process (P1–P4), the finer feedstock powder (W1-series) produces coatings with slightly higher toughness and elastic modulus than those obtained from the coarser one (W2-series). Once again, this is obvious for elastic modulus data, whilst the significance of the differences between pairs of K_{IC} values is confirmed by the Student's *t*-test (Fig. 6A). With each spray process, the finer powder therefore provides better interparticle cohesion. The finer powder particles probably exhibit better plastic flow behaviour upon impact onto the substrate. Particles therefore spread out more extensively, creating stronger interfaces with fewer defects.

It is also noted that the present indentation fracture toughness values of $\approx 4\text{--}7 \text{ MPa} \cdot \text{m}^{1/2}$ (Fig. 6) are consistent with literature values computed for similar WC-based coatings using the same equation [55–58].

Comparison of Vickers microhardness measurements at 300 gf and 500 gf load (with the aid of the *p*-values from Student's *t*-test provided in the supplementary data) also reveals a decrease from the W1-series to the W2-series sample, which is related to weaker long-range cohesive strength. Large material volumes, including a number of splats, are indeed affected at such indentation loads [59].

Microhardness at low loads, by contrast, is mainly affected by intra-lamellar properties; therefore, the significantly higher $HV_{0.1}$ values of the HVOF-sprayed samples obtained from the fine feedstock powder (P2W1, P3W1) compared to those obtained from the coarse one (P2W2, P3W2) is probably related to the greater carbide dissolution observed in the former (Section 3.2 and Table 2), which increases the hardness and brittleness of the matrix phase. Accordingly, the HVOF-sprayed samples, which never undergo measurable losses of WC phase (Section 3.2 and Table 2), exhibit no significant change in $HV_{0.1}$ values with coarsening of the feedstock powder (compare samples P1W1 to P1W2 and P4W1 to P4W2: Fig. 5 and *p*-values table in the supplementary data).

As the test load increases, microhardness starts being somewhat affected by inter-lamellar cohesion as well. Stronger large-scale inter-lamellar cohesion in the samples obtained from the fine feedstock powder is therefore also proven by the fact that the distribution of hardness data in the W1-series samples becomes narrower with increasing

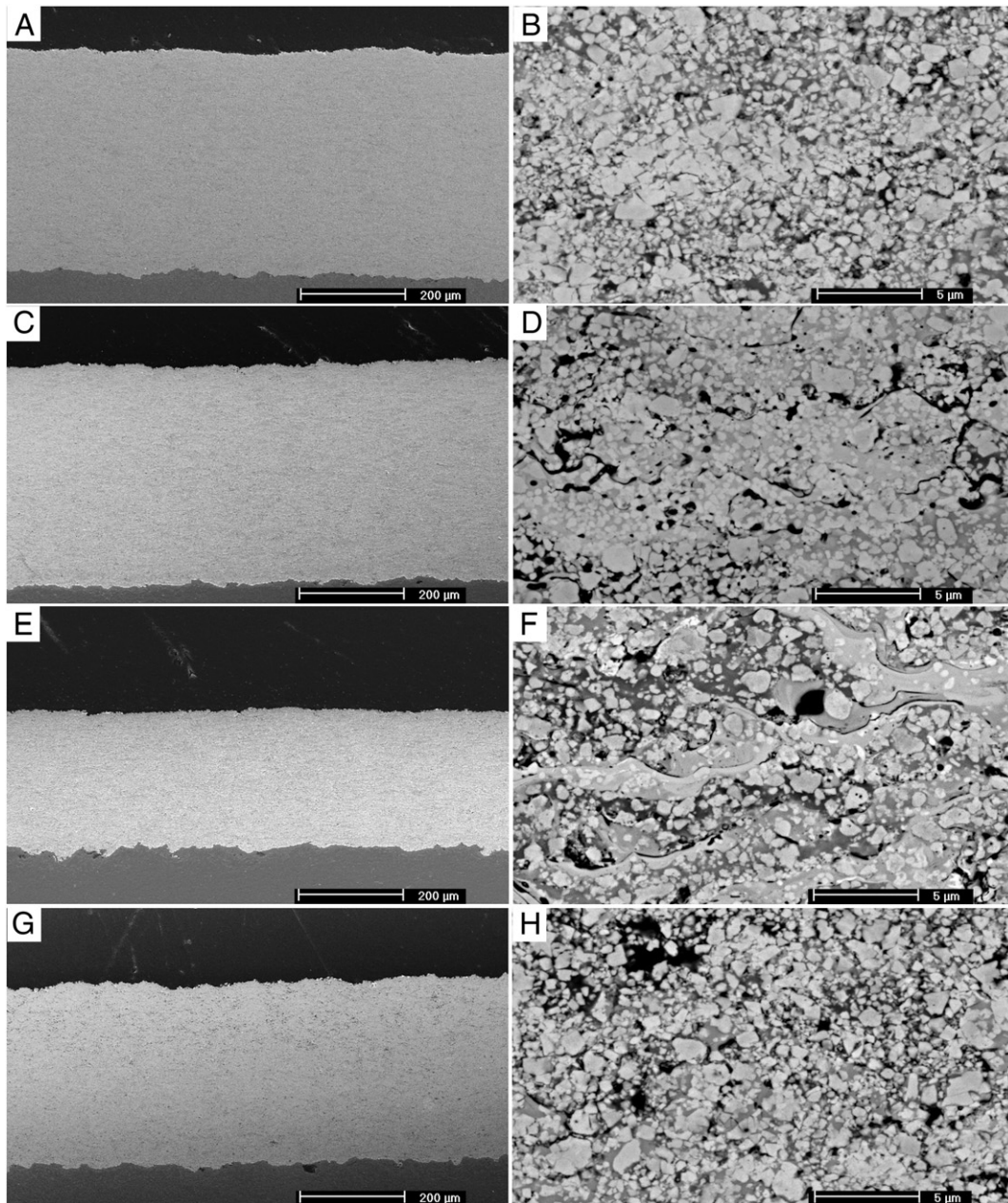


Fig. 4. Cross-sectional SEM micrographs of samples P1W1 (A,B), P2W1 (C,D), P3W1 (E,F), and P4W1 (G,H).

indentation load (Fig. 5A). In the coatings belonging to the W2-series, by contrast, the distribution of experimentally measured hardness values remains considerably broad from 100 gf to 500 gf (Fig. 5B).

Table 2

Index of carbide retention (*I*) of all hardmetal coatings; porosity, volume fractions of matrix and of WC grains and average size of the latter, assessed by image analysis on SEM micrographs (Section 2.2); and resulting values of computed density (Section 2.3).

Sample	Porosity (vol.%)	Carbides (vol.%)	Carbide size (μm)	Binder (vol.%)	Density (g/cm ³)	Index of WC retention (<i>I</i>)
P1W1	0.7 ± 0.5	54.9 ± 9.0	0.7 ± 0.1	44.4 ± 8.9	12.4	>98%
P1W2	2.1 ± 1.7	51.3 ± 7.0	0.8 ± 0.1	46.6 ± 6.6	12.1	>98%
P2W1	3.9 ± 1.9	49.5 ± 4.7	0.6 ± 0.1	46.6 ± 4.7	11.8	60%
P2W2	4.1 ± 1.8	47.3 ± 5.9	0.6 ± 0.1	48.6 ± 5.5	11.6	84%
P3W1	2.0 ± 0.9	63.3 ± 9.5	0.8 ± 0.2	34.7 ± 9.3	12.9	54%
P3W2	7.3 ± 3.3	57.8 ± 8.5	0.8 ± 0.1	34.9 ± 7.7	12.1	83%
P4W1	1.1 ± 1.0	72.9 ± 2.9	1.2 ± 0.2	26.0 ± 2.5	13.7	>98%
P4W2	1.8 ± 1.6	67.4 ± 3.3	1.1 ± 0.2	30.8 ± 2.2	13.2	>98%

This is mostly due to the presence of a comparatively higher amount of defects (resulting in increasing inter-lamellar sliding at higher loads) and to greater local variability (e.g. particles with different flattening and/or melting degrees) in the coatings of the W2-series, compared to the ones obtained from the finer powder W1.

3.4. Ball-on-disk testing

3.4.1. Room temperature behaviour

At room temperature, the sliding wear rates of all WC–10Co4Cr coatings (Fig. 7) are below 10^{-7} mm³/(Nm), i.e. they correspond to a mild wear regime [60]. Under the present experimental conditions, they are orders of magnitude lower than those of electroplated hard chromium references. The differences between the various WC–10Co4Cr coatings are small and often negligible within experimental error, as the probability of the “null hypothesis” from the Student’s *t*-test is $p > 0.05$ for many of the data pairs (see the related table in Fig. 7). Most of the statistically significant differences concern samples P2W1 and,

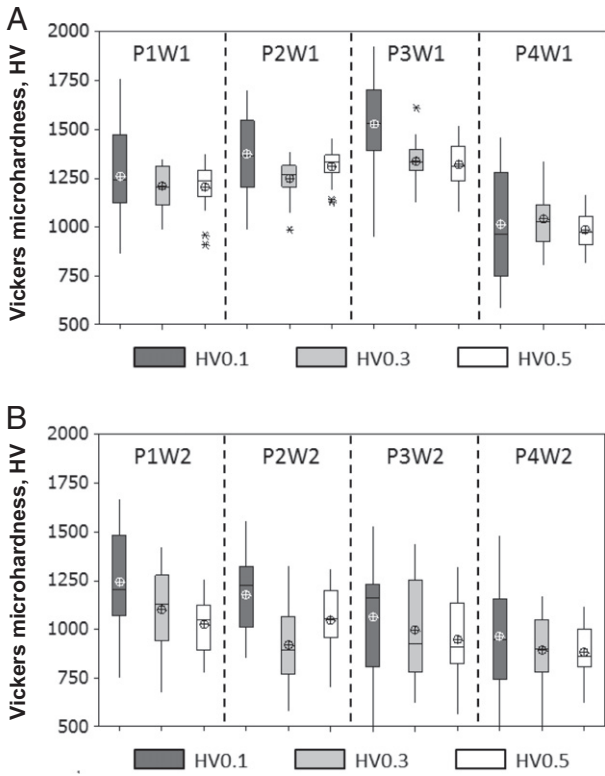


Fig. 5. Vickers microhardness results: boxplot representation of the distribution of 20 hardness values per coating following ASTM E-384-10, for samples belonging to the W1- (A) and W2- (B) series.

particularly, P3W1. They indeed exhibit slightly higher wear rates than all other samples, which can be interpreted based on the following analysis of wear mechanisms.

The WC-10Co4Cr coatings exhibit a combination of two concurrent wear mechanisms:

- (i) Near-surface plastic deformation, leading to the formation of rough “waves” (Fig. 8, label 1) consisting of lips of material extruded out of the surface (Fig. 9C,D). Friction between the mating bodies induces a shear stress on the coating surface, directly on the contact area with the counterpart, which causes out-of-plane plastic flow of the metal matrix at an angle of approximately 45° with respect to the pristine surface plane. The WC grains, due to their fine size (micrometric and sub-micrometric, see Section 3.1), are dragged together with the matrix into these “wavy” extrusions. These “waves” have a micrometric length scale, hence the plastic flow phenomena probably occur at the intra-lamellar level.
- (ii) Brittle cracking, which leads to the detachment of small portions of material from the coating surface (Fig. 8, label 2). This mechanism is probably mainly responsible for the largest part of the wear loss. The size of cracks and of the resulting voids left on the coating surfaces, ranging mostly from few micrometres to few tens of micrometres (Fig. 9A,B), is usually smaller than the size of splats formed from the feedstock powder particles. Cracking during sliding contact, under the present test conditions, is therefore taking place at the intra-lamellar level, i.e. inside individual lamellae.

Both mechanisms occur simultaneously for all coatings: e.g., see Fig. 9A and 9D showing two different details of the same worn surface. Their respective contributions to the wear loss, however, differ in the various samples. As they both take place at intra-lamellar level (which is probably due to the small size of the contacting asperities on the mating bodies), their relative incidence is primarily determined by intra-lamellar properties. As a result, crack formation and propagation are more likely to occur on coatings which have been embrittled at the intra-lamellar scale by carbide dissolution and by carbon deficiency, such as samples P2W1 and P3W1 (see Section 3.2 and Table 2). Coating properties at the inter-lamellar level (i.e. on a larger length scale) have comparatively lower relevance. This is supported by the fact that the wear rates of the coatings sprayed with the M2-HVAF process (P4W1, P4W2) are lower than those of samples P2W1 and P3W1 and comparable to those of all other WC-10Co4Cr coatings, although their inter-

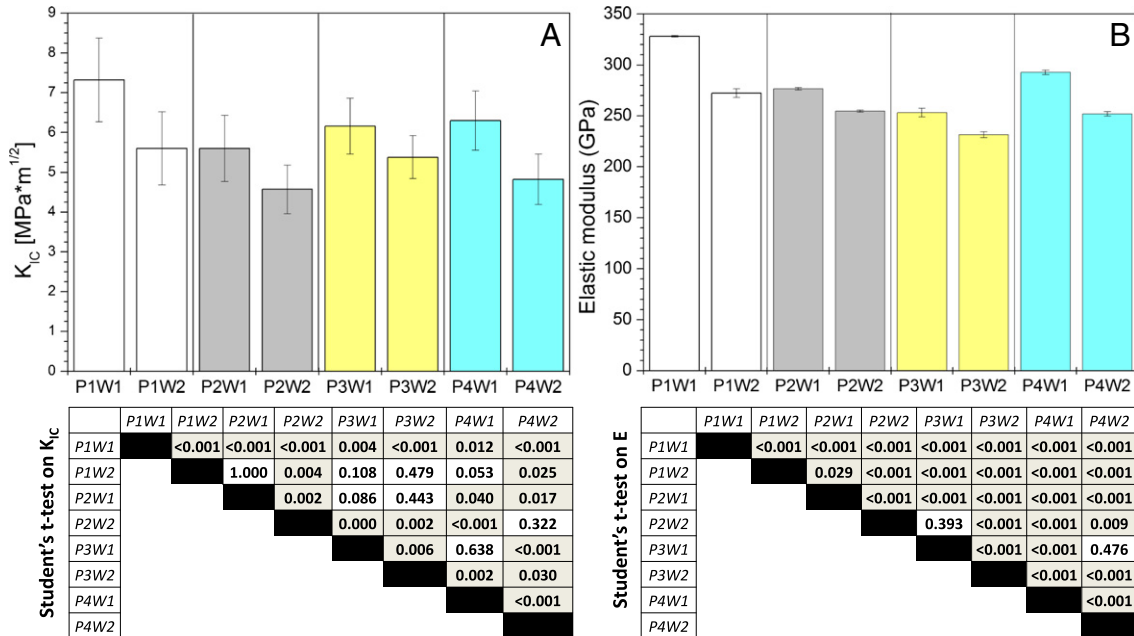


Fig. 6. (A) Indentation fracture toughness (K_{1c}) and (B) elastic modulus values of all coatings, with corresponding matrices of p-values from Student's t-test. Sample pairs with p < 0.05 are assumed to have significantly different average values and are highlighted in grey colour, whereas those with p ≥ 0.05 may have identical averages and are highlighted in white colour.

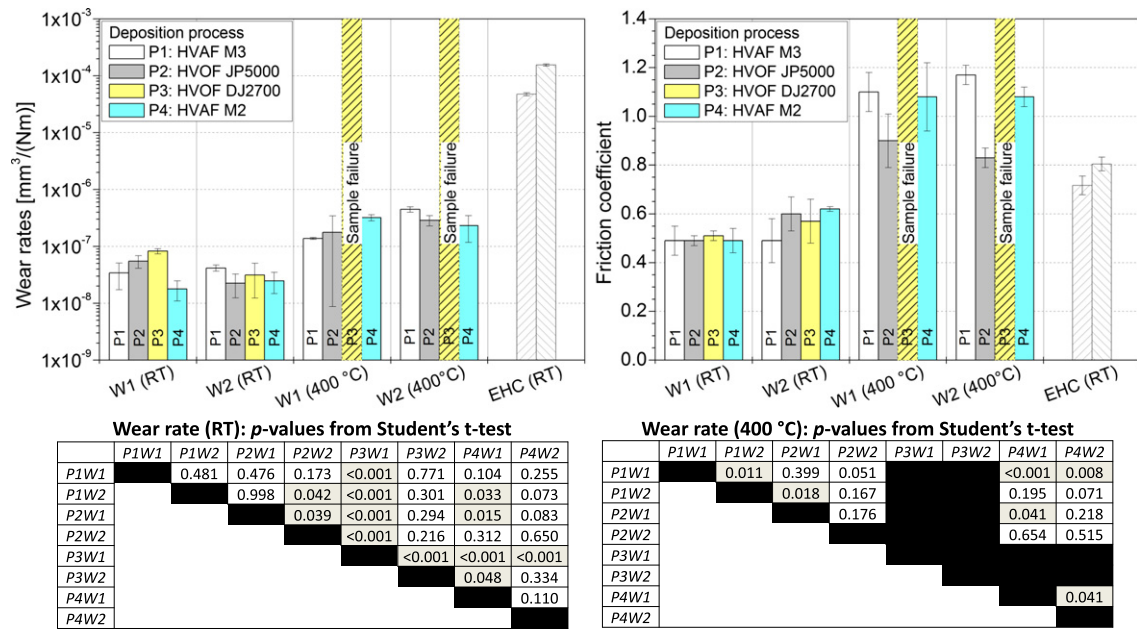


Fig. 7. Wear rates and friction coefficients obtained by ball-on-disk dry sliding wear tests at room temperature (RT) and at 400 °C. Matrixes of *p*-values from Student's *t*-test are provided for wear rate data at room temperature and at 400 °C. Sample pairs with *p* < 0.05 are assumed to have significantly different average values and are highlighted in grey colour, whereas those with *p* ≥ 0.05 may have identical averages and are highlighted in white colour.

lamellar cohesion is poorer, as discussed in Section 3.3 based on hardness and toughness measurements (Figs. 5 and 6).

These qualitative considerations are statistically supported by principal component analysis (PCA). The PCA method devises a set of *n* orthogonal vectors (the principal components), which represent a

basis for the *n*-dimensional space constituted by a set of *m* measurements of *n* distinct variables. Of the infinite available orthogonal bases, PCA computes the one which best describes the variance of the data set. Namely, the first principal component accounts for the highest possible fraction of the overall variance of the data set, the second one accounts for the highest fraction of the remaining variance, etc. Each principal component is therefore a linear combination of the original variables.

In the present case, the selected variables are porosity and carbide content (from image analysis), index of carbide retention (from XRD peak fitting), Vickers microhardness measured with 100 gf (HV_{0.1}) and 500 gf loads (HV_{0.5}), indentation fracture toughness (K_{IC}), elastic modulus (E), and sliding wear rate at room temperature. They provide a (*m* = 8) × (*n* = 8) matrix of experimental observations.

By applying the PCA method, a set of orthogonal principal components is devised, where the first and second ones alone account for about 80% of the variance of the data set (see the Pareto chart in Fig. 10A), whilst all components from the 5th to the 8th are basically insignificant. The following analysis will therefore focus on the first and second principal components only. The contributions of the original variables to these components are plotted as vectors in Fig. 10B, together with the coordinates of each data point (i.e. of each of the eight WC-CoCr coatings) in the new reference system. The amount of carbides (measured both by the index of carbide retention and by the carbide content) and the microhardness at low load (HV_{0.1}) are the variables which correlate best with the sliding wear rate.

The index of carbide retention and the sliding wear rate indeed provide nearly opposite contributions to the 1st and 2nd principal components, which means a decrease in carbide retention translates almost directly into an increase in sliding wear rate, in accordance with the previous discussion. Similar considerations hold for the carbide content, although carbide retention and carbide content are not coincident (Fig. 10B), which probably comes from their different measurement methods (XRD peak fitting vs. image analysis).

Analogously, wear rate and HV_{0.1} have similar (though not identical) contributions to both of the principal components. It was accordingly observed in Section 3.3 that HV_{0.1} largely reflects intra-lamellar properties; in particular, it is affected by carbide dissolution. As the latter increases, the intra-lamellar material grows harder but it also loses

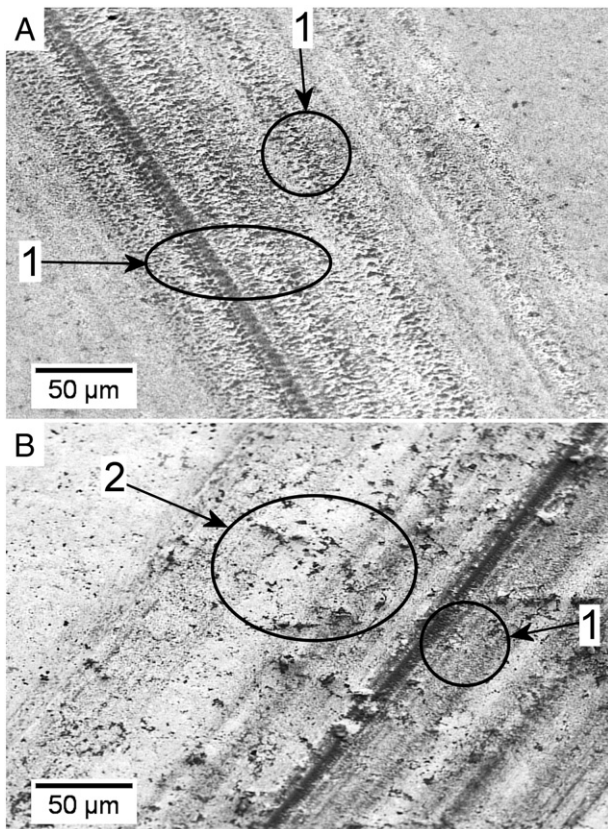


Fig. 8. SEM micrographs of the wear scars on samples P1W1 (A) and P2W2 (B). Label 1 = plastically deformed “wavy” features; label 2 = areas with evidence of brittle cracking.

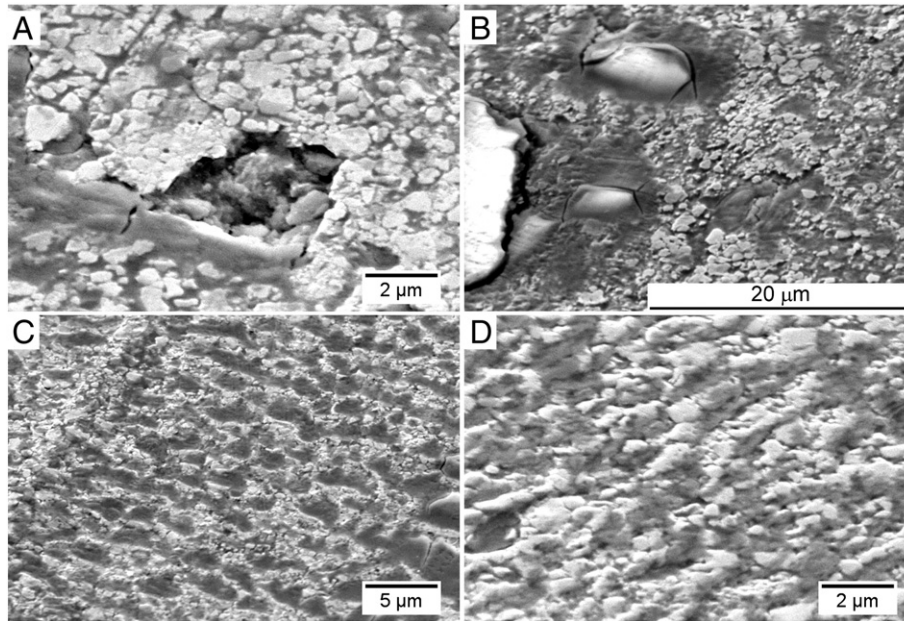


Fig. 9. High magnification SEM micrographs of the wear scars of samples P2W2 (A) and P3W1 (B), showing details of brittle cracking regions, and of samples P1W2 (C) and P2W2 (D), showing details of plastically deformed “wavy” areas.

toughness, thus becoming more prone to wear by micro-scale brittle fracture (as mentioned previously), resulting in higher wear rates as quantitatively shown by Fig. 10B. The relation between the sliding wear rate and the $HV_{0.5}$ value is less obvious, as the latter bears a greater influence from inter-lamellar cohesion (see Section 3.3), which has no significant role on sliding wear.

The wear rate is indeed almost orthogonal to the elastic modulus and to indentation fracture toughness. This leads to the following considerations:

- (i) The elastic modulus measured by the acoustic-wave propagation technique and the indentation fracture toughness obtained by

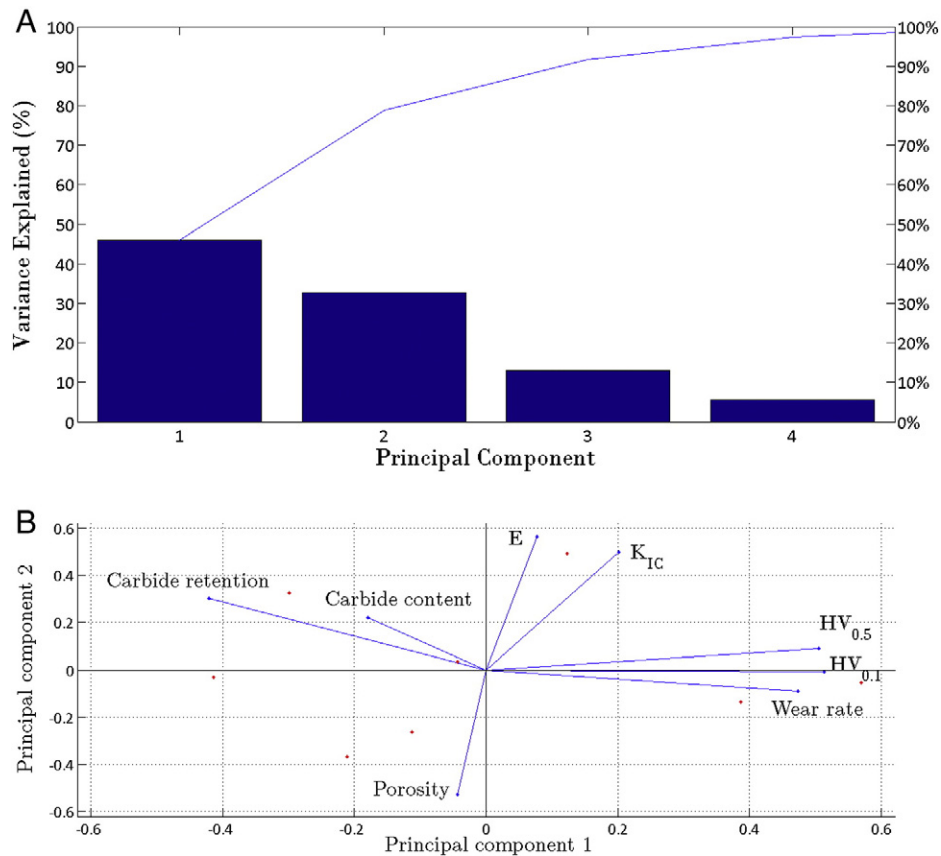


Fig. 10. Results of principal component analysis for sliding wear at room temperature: (A) Pareto chart, and (B) plot of the variable coefficients (vectors) and of the observation scores (dots) along the 1st and 2nd principal components.

high-load indentation testing are closely related to one another as they both primarily measure large-scale inter-lamellar cohesion (as previously explained in Section 3.3);

- (ii) Inter-lamellar properties are not influential on the sliding wear behaviour, in accordance with the previous observations.

After plastic flow has occurred, the matrix is removed from the extruded lips, so that WC grains are soon protruding on top of the “waves”, as seen in Figs. 9C,D. Following an initial running-in period, most of the contact is therefore borne by the WC grains alone. Due to their hardness, their tendency to stick to the alumina counterpart is low, so that no adhesion and no material transfer between the mating bodies occurs, consistent with the smooth and quite clean wear surface of the alumina counterpart (Fig. 11A,B). The latter undergoes mild polishing wear at a rate of $\leq 10^{-8}$ mm³/(Nm), lower than that of all WC–10Co4Cr coatings by up to one order of magnitude (in accordance with previous studies on similar material pairings [51,61]). The resulting friction coefficients are approximately 0.5 (Fig. 7): they are not particularly low, but they indicate that no seizure occurs between the contacting surfaces.

As the wear loss of both the WC–10Co4Cr coatings and the counterpart is confined to a mild wear regime, very fine debris is produced, consisting of aggregates of nanometric particles (Fig. 12A) with an amorphous structure, as seen in high resolution TEM micrographs and in the corresponding SAED patterns (Fig. 12B). The Raman spectrum of this debris (Fig. 13) is similar to that of amorphous Co/W oxides with high W content [62]. This Co-containing amorphous W oxide is

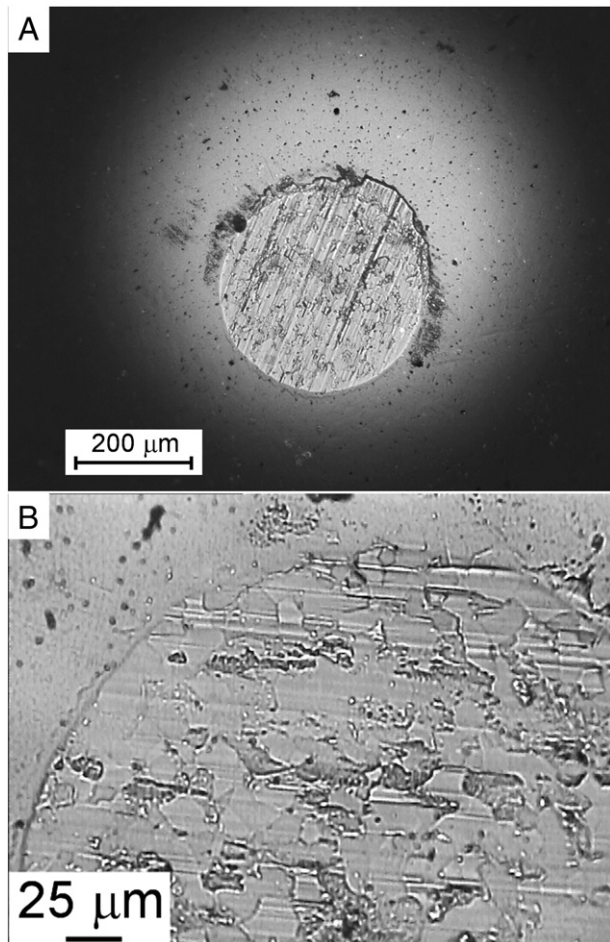


Fig. 11. Optical micrographs of the worn surface of the alumina ball after sliding at room temperature against WC–CoCr samples P1W1 (A) and P3W2 (B).

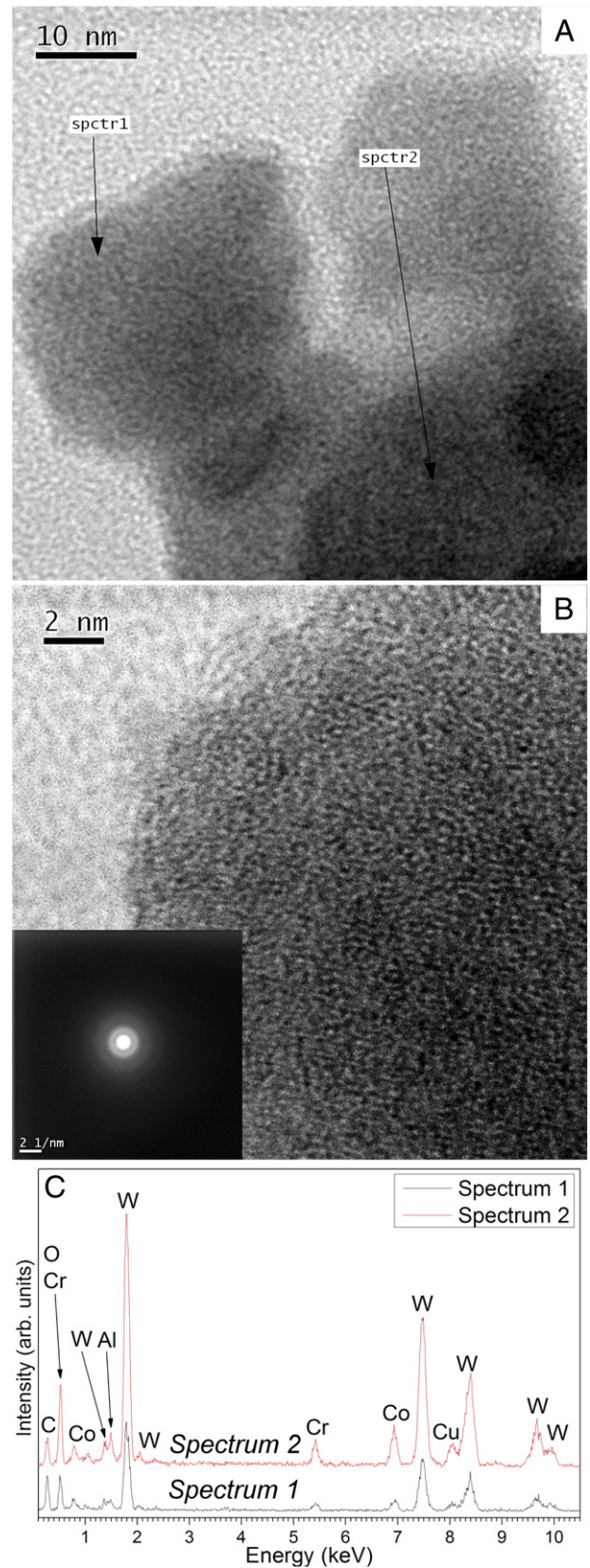


Fig. 12. TEM micrographs of the loose wear debris collected outside the wear scar after ball-on-disk sliding wear testing on sample P1W2 (A,B), with inset SAED pattern, and EDX spectra acquired at the locations marked in panel A (D). Note that the EDX peak of Cu is due to the contribution of the copper grid supporting the sample.

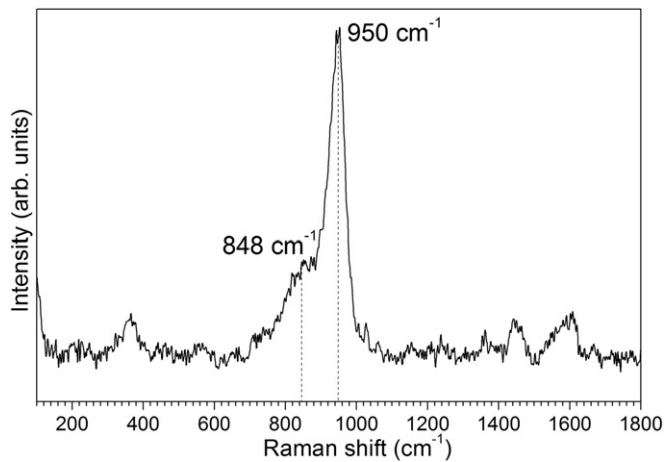


Fig. 13. Raman spectra of the loose wear debris collected outside the wear scar after ball-on-disk sliding wear testing on sample P1W2.

formed by comminution and tribo-oxidation of very small fragments of coating material, coming either from the removal of the metal matrix together with a few WC grains during lip extrusion and “waves” formation (mechanism i), or from brittle cracking (mechanism ii). In [63], amorphous W-based oxide was also reported as the main constituent of the wear debris of bulk WC–Co in fretting contact against alumina. Very little Al is found in the debris (Fig. 11C), as the wear loss of the Al_2O_3 counterpart was previously shown to be one order of magnitude lower than that of the coating.

In the case of electrolytic hard chromium coatings, by contrast, more severe wear occurs by abrasion (Fig. 14A) and adhesion (as indicated by the small delaminations seen in Fig. 14B). Accordingly, the coating sticks to the counterbody and builds a transfer layer onto it (Fig. 14C), resulting in much higher friction coefficient than that produced by WC–10Co4Cr under the same experimental conditions (Fig. 7). Debris particles are also much bigger (Fig. 15A). They are partly crystalline (Fig. 15B and SAED pattern in Fig. 15C) and, based on the low intensity of the oxygen peak in the corresponding EDX spectra (Fig. 16A – note that this peak is also partly overlapped by the Cr–L lines), they are probably not completely oxidised, i.e. they contain quite coarse fragments of chromium. The presence of an oxidised fraction is however indicated by the possibility to acquire well-defined Raman spectra (Fig. 16B). Straightforward interpretation of these spectra is not easy: the broad feature at $\approx 550\text{ cm}^{-1}$ can be ascribed to Cr(III) oxi-hydroxides [64], but the main peak at $\approx 880\text{ cm}^{-1}$ may belong either to chromate species [64] or to Cr_2O_3 nanoparticles with hydroxylated surfaces [65]. The possible release of chromates in the debris, as a result of wear and tribo-oxidation of electroplated hard chromium in sliding contacts, has not been examined in the literature up to now, and it cannot be undoubtedly claimed based on the present results. Deeper investigation on this topic is outside the aim of this work, but it should be carried out in future research. If the finding of Cr(VI) in the debris is confirmed, indeed, it would constitute another important health and safety issue calling for the replacement of electroplated hard chromium.

3.4.2. Behaviour at 400 °C

At 400 °C, the wear rates of WC–10Co4Cr coatings increase by one order of magnitude and become somewhat higher than $10^{-7}\text{ mm}^3/(\text{Nm})$ (Fig. 7), with the exception of samples P3W1 and P3W2, which failed due to the development of a macroscopically visible network of through-thickness cracks across their entire surface (Fig. 17). The cracks, which propagate with a somewhat tortuous path across the coating, often reaching down to the substrate (Fig. 18B), were probably formed as the sample reached the test temperature, before the sliding test was commenced, so that ball and sample wear rates are not meaningful in this case.

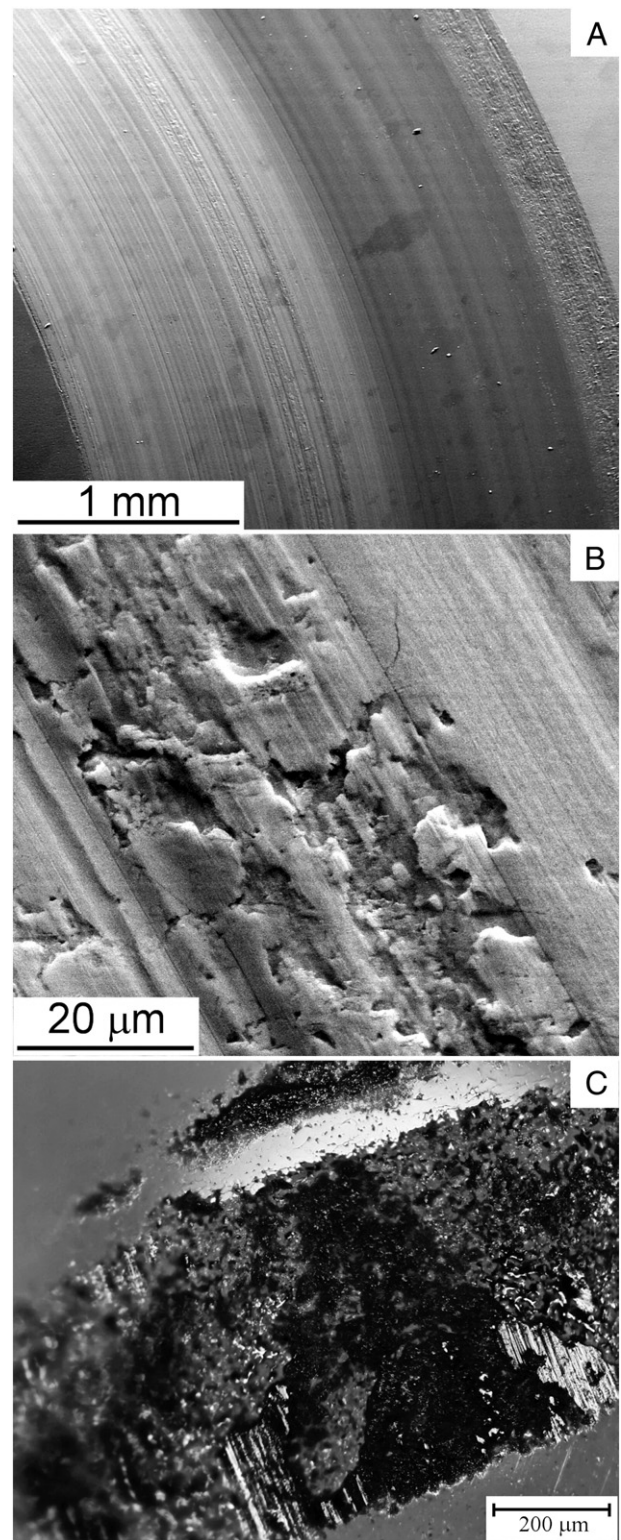
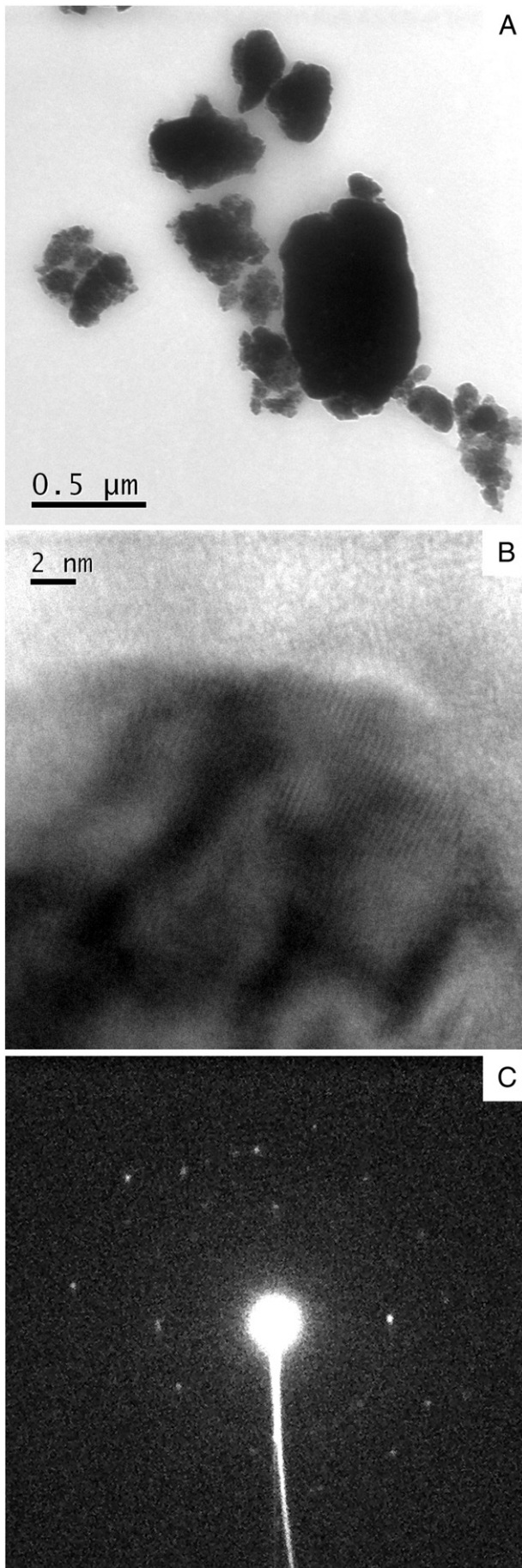


Fig. 14. SEM micrographs showing an overview (A) and a detail (B) of the wear scar produced after ball-on-disk testing on electroplated hard chromium at room temperature, and optical micrograph of the corresponding wear scar on the Al_2O_3 ball (C).

3.4.2.1. Analysis of crack formation. The formation of cracks in the samples deposited by the P3 process (namely, Diamond Jet 2700 HVOF spraying) is probably due to a number of superimposed factors, including (a) precipitation of secondary carbides, (b) development of thermal expansion mismatch stresses and (c) presence of residual stresses, as explained below.



(a) The microstructure of the HVOF-sprayed samples does not change after high-temperature exposure (Fig. 18A,C). In the HVOF-sprayed coatings, on the other hand, few secondary bright (W-rich) phases appear in the form small, irregularly-shaped precipitates, often located around some of the original WC grains (see circled areas in Fig. 18D). Most probably, W-based secondary carbides precipitated from the matrix, which contained W and C because of the dissolution of WC during HVOF spraying, as discussed in Section 3.2. Such precipitation has accordingly been observed in some previous works, though at somewhat higher temperatures [66,67]. This phenomenon alone, however, cannot account for the appearance of cracks, which affects only the samples deposited with one of the two HVOF processes.

(b) In the temperature range from 30 °C to 400 °C, the thermal expansion coefficient of WC–10Co4Cr is less than half of that of the substrate (Table 3). The experimentally measured CTE values listed in Table 3 are qualitatively in a good agreement with those measured for HVOF-sprayed WC–17 wt.% Co by Thiele et al. [42]. As the sample reaches the test temperature of 400 °C, the coating becomes subject to significant tensile stresses, an analytical estimate of which can be obtained using the composite beam theory as laid out e.g. in [68]. Specifically, two opposite normal forces (F_T) act on the coating and on the substrate due to thermal expansion mismatch (Fig. 19), and a bending moment (M_T) arises to balance the normal forces torque. The thermal expansion mismatch stresses on top of the coating layer ($\sigma_{y=h}^T$) and at the coating-substrate interface ($\sigma_{y=0}^T$) are therefore computed as the sum of the contributions due to the normal force and to the bending moment:

$$\sigma_{y=h}^T = \frac{F_T}{bh} - E_C \kappa (h - \delta) \quad (3.1)$$

$$\sigma_{y=0}^T = \frac{F_T}{bh} - E_C \kappa \delta \quad (3.2)$$

with:

$$\delta = \frac{E_C h^2 - E_S H^2}{2(E_C h + E_S H)} \text{ neutral axis position}$$

$$\kappa = M_T / \Sigma \text{ curvature of the coated system}$$

$$\Sigma = bhE_C \left(\frac{h^2}{3} - h\delta + \delta^2 \right) + bHE_S \left(\frac{H^2}{3} + H\delta + \delta^2 \right) \text{ flexural stiffness}$$

$$M_T = F_T \frac{H+h}{2} \text{ bending moment}$$

$$F_T = b(\alpha_S - \alpha_C) \Delta T \frac{HhE_S E_C}{hE_C + H E_S} \text{ normal force}$$

With reference to the diagram in Fig. 19: b = out-of-plane sample width (= 50 mm); h = coating thickness (≈ 0.35 mm, see Section 2.1); H = substrate thickness (= 8 mm); ΔT = temperature change = (400–20) °C = 380 °C; α_S , α_C = thermal expansion coefficients of the substrate and of the coating (from Table 3).

The elastic modulus of the steel substrate is $E_S = 210$ GPa, whereas that of HVOF-sprayed WC–10Co4Cr coatings (E_C), as shown in Fig. 5B, is approximately comprised in the 250–300 GPa range; therefore, from Eqs. (3.1) and (3.2) it follows: $\sigma_{y=h}^T = 566$ –654 MPa, $\sigma_{y=0}^T = 574$ –665 MPa.

Since the thermal expansion coefficient is not strongly dependent on the microstructure of a coating, it can be quite confidently assumed that the values in Table 3 and, therefore, the above thermal stress estimates are representative of all WC–10Co4Cr coatings employed in this study.

(c) As the crack network only affects the samples deposited by the Diamond Jet HVOF process, the thermal expansion mismatch is not its only cause. Notably, in a previous study [28],

Fig. 15. TEM micrographs of the wear debris produced after ball-on-disk testing of the electroplated hard chromium layer at room temperature (A: overview; B: detail) and corresponding selected area diffraction pattern acquired on the area shown in panel B (C).

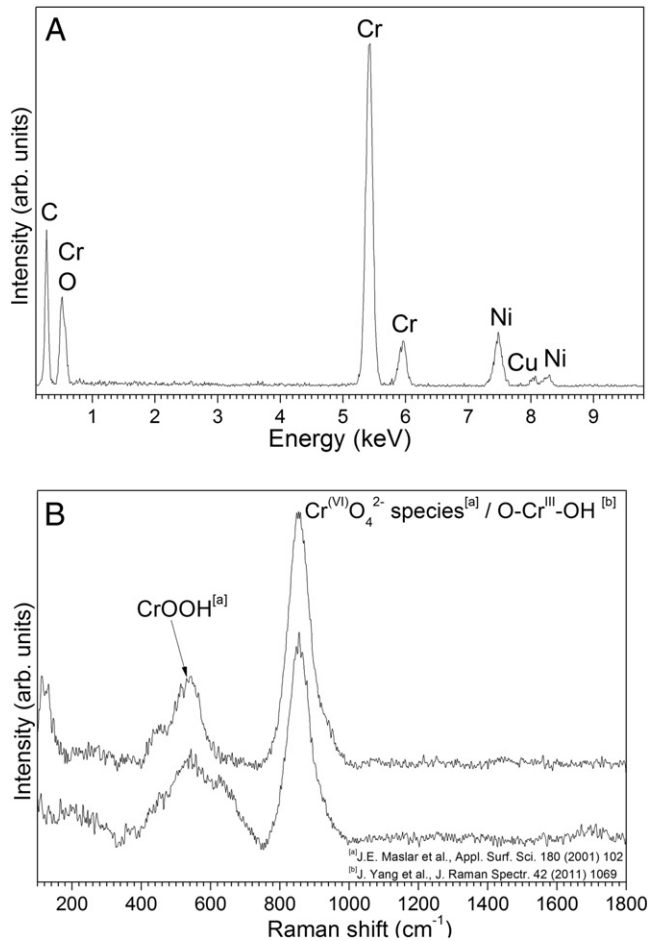


Fig. 16. EDX spectra (A) and Raman spectra (B) acquired on the wear debris produced by ball-on-disk testing of electroplated hard chromium at room temperature.

other WC–10Co4Cr coatings sprayed by Diamond Jet 2600 process, using hydrogen as fuel gas, onto carbon steel developed an analogous macro-crack network upon heating to 500 °C. The systematic recurrence of the phenomenon in coatings deposited by this specific process suggests the occurrence of some additional deposition-related factor. Decarburisation during spraying and consequent high-temperature precipitation of secondary phases during testing is also not a viable explanation, as discussed in point a). The cause more reasonably lies in the residual stress state of the coatings.

X-ray residual stress analysis was therefore performed on the samples deposited with fine powder feedstock (W1 series). The results (Table 4) clearly show that, compared to the other coatings, sample P3W1 is subject to significantly higher tensile residual stresses on its top surface. Overall stress levels as high as 900–1000 MPa in the samples deposited by the Diamond Jet HVOF process can therefore result from the superposition of their residual stresses, listed in Table 4, with thermal expansion mismatch stresses previously estimated at point (b). Such stress levels are obviously capable of inducing extensive cracking of the P3-series coatings.

The JP5000-HVOF-sprayed coating (sample P2W1) is subjected to comparatively lower tensile residual stresses on its top surface: this is probably due to the higher impact velocity of particles sprayed by liquid-fuelled HVOF processes, inducing greater peening effects which partly balance the tensile quenching stress contribution [69].

In the HVOF process, stronger peening effects and less splat quenching result in almost zero residual stress on the top surface.

The stress values of samples P1W1 and P4W1 as listed in Table 4 are indeed almost of the same order of magnitude of the accuracy of the X-ray residual stress measurement technique, which is usually of ≈ 20 MPa.

3.4.2.2. Analysis of wear mechanisms. All non-failed samples (P1, P2 and P4 series) have quite similar wear rates at 400 °C; indeed, only few of the *p*-values from Student's *t*-test are below the statistical significance threshold of 0.05, and almost none falls below 0.01 (see the related table in Fig. 7). Accordingly, all of their wear mechanisms are substantially similar, and they differ remarkably from those appearing at room temperature (Section 3.4.1). This is consistent with the previously reported order-of-magnitude increase in wear rates (Fig. 7). Specifically, the wear scars bear evidence of more severe abrasive grooving (Fig. 20A), affecting the WC grains as well (Fig. 20B,C).

The hardness of WC is reported to be nearly constant in the temperature range up to 400 °C [70,71]. However, SEM micrographs (Fig. 21A) and AFM maps (Fig. 21B) acquired outside the wear scar show that WC grains not covered with the metallic binder developed oxide protrusions consisting of WO₃ (see Raman spectrum in Fig. 21C), whilst the matrix remained relatively unaffected. Due to its specific volume being much larger than that of WC, WO₃ adheres poorly to the underlying carbide grain and grows with significant defects [72], so it is expected to be easily removed during sliding. Permanent removal of the WO₃

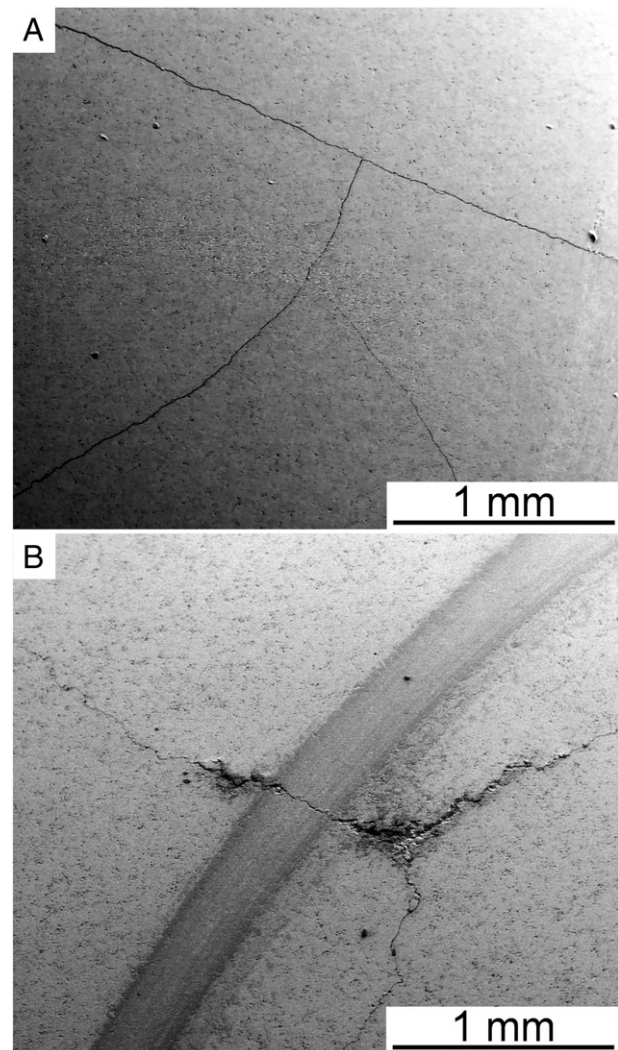


Fig. 17. SEM micrographs of the top surfaces of samples P3W1 (A) and P3W2 (B) after ball-on-disk wear testing at 400 °C.

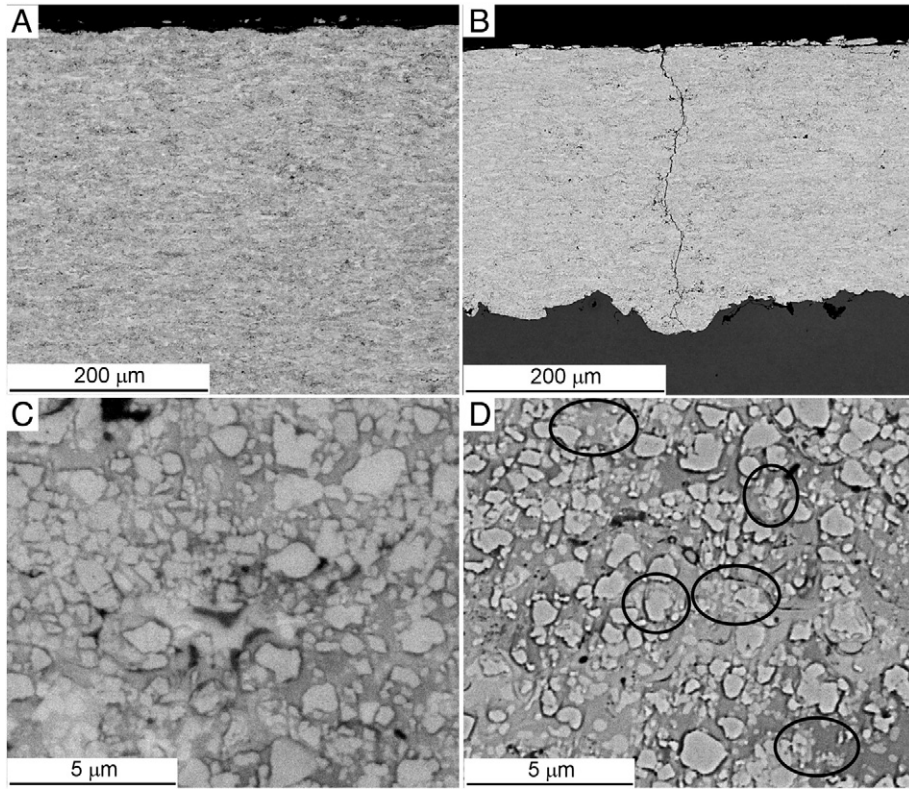


Fig. 18. SEM micrographs of the polished cross-sections of samples P1W2 (A: low-magnification, C: high magnification) and P3W1 (B: low-magnification, D: high magnification) after ball-on-disk wear testing at 400 °C. The circles in panel D indicate areas with visible precipitates around the WC grains.

scale and ongoing fast oxidation of WC grains are therefore plausible causes for the observed abrasive grooving.

The carbide grains therefore become unable to prevent the coating from sticking to the alumina counterbody. Evidence of adhesive wear is indeed found, with material being torn out of the coating surface (Fig. 20D), and a transfer layer is built up on the counterpart (Fig. 22). Adhesive wear and the consequent onset of self-mated contact between the coating and the transfer layer account for the high friction coefficient recorded at this temperature (usually around 1, Fig. 7).

Friction induces tensile stresses on the coating surface, behind the contact region: the coupling of this stress to the thermal expansion mismatch stress discussed in Section 3.4.2.1 results in transverse microcracking across the entire wear scar (Fig. 20B,C: see arrows). Consistent observations were reported by the authors in a previous study [29]. Such cracks were not found in the wear scars of HVOF-sprayed WC–FeCrAl coatings tested at the same temperature in that study [29], in spite of its thermal expansion coefficient [29] being practically identical to that of the present WC–10Co4Cr samples. This indicates that some form of high-temperature brittleness also contributes to making WC–10Co4Cr unable to withstand the combined action of these stresses.

Table 3
Coefficient of thermal expansion of WC–CoCr and of the Domex 355 steel substrate as a function of temperature, from optical dilatometer measurements.

Temperature range [°C]	CTE [$\times 10^{-6} \text{ } ^\circ\text{C}^{-1}$]	
	WC–CoCr	Domex 355 steel
30–100	6.59	12.59
30–200	6.72	13.27
30–300	6.81	13.82
30–400	6.90	14.23

3.5 . Dry sand–rubber wheel testing

Volume losses after dry sand–rubber wheel testing were computed from mass losses using the density values listed in Table 2, as described in Section 2.3. The ranking of the various WC–10Co4Cr coatings in this test (Fig. 23) is different from sliding wear conditions at room temperature and clearly depends on the feedstock powder particle size. Namely, the coatings obtained from the coarse feedstock powder (W2-series) experience somewhat larger volume losses than those obtained from the fine powder (W1-series).

The factors underlying this behaviour can be interpreted with the aid of PCA results. In addition to the abrasive volume loss (Fig. 23), the chosen variables, as in Section 3.4.1, are porosity, carbide content,

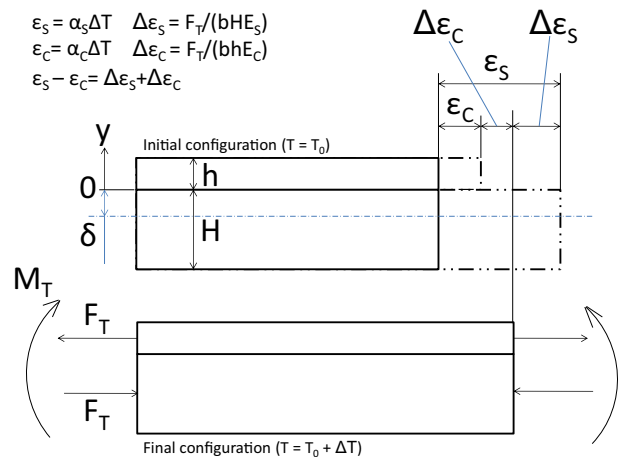


Fig. 19. Schematics of thermal stress build-up in the coating–substrate system.

Table 4

Residual stresses in W1-series samples, measured by X-ray diffraction using equation set (1) (Section 2.4).

Direction 1 is parallel to the long side of the 100 × 50 mm rectangular plates; direction 2 is parallel to the short side.

Sample	σ_{11} [MPa]	σ_{22} [MPa]	τ_{12} [MPa]
P1W1 (HVOF)	91	2	44
P2W1 (HVOF)	57	148	9
P3W1 (HVOF)	328	282	23
P4W1 (HVOF)	−23	59	−61

index of carbide retention (Table 2), $HV_{0.1}$, $HV_{0.5}$ (Fig. 5), elastic modulus and K_{IC} (Fig. 6). Once again, focus can be placed on the first and second principal components only, as they jointly account for around 80% of the overall variance (Pareto chart in Fig. 24A). The contributions of the different variables to such components (Fig. 24B) depict a completely opposite situation, as compared to the sliding wear results in Section 3.4.1. The abrasive volume loss is poorly related or even almost orthogonal (i.e. unrelated) to the variables (index of carbide retention, carbide content, $HV_{0.1}$) which were the most influential on the sliding wear rate. Instead, it is closely connected to parameters which measure long-range inter-lamellar cohesion (elastic modulus and indentation fracture toughness) and microstructural defectiveness (porosity).

It is therefore concluded that intra-lamellar properties, which controlled the sliding wear behaviour, are largely irrelevant for the abrasive wear resistance. The latter benefits the most from high coating density and strong inter-lamellar cohesion.

This behaviour is explained by the two main wear mechanisms controlling the dry particle abrasion of these materials, identified by SEM micrographs of the wear scars (representative overviews in Fig. 25A, B). On one hand, the binder matrix is abraded until the unsupported WC grains are cracked and pulled out of the surface, as observed e.g. in Fig. 25C. On the other hand, larger portions of material are detached from the surface by brittle fracture (see circled areas in Fig. 25A,B; detail

in Fig. 25D). Similar mechanisms of matrix abrasion and brittle fracture were also reported in various previous studies [30,73–75]. Brittle fracture, which is clearly responsible for the greater part of the wear loss, appears more frequently for coatings deposited from the coarse feedstock powders (compare Fig. 25B to Fig. 25A).

The size of these delaminated regions, ranging from some tens of micrometres up to $\approx 100 \mu\text{m}$, matches with the expected size of lamellae obtained by deformation and flattening of the impacting feedstock powder particles. It is therefore inferred that brittle removal of entire lamellae is taking place (as previously reported in [75]); namely, the resistance to dry particle abrasion largely depends on inter-lamellar cohesion, differently from ball-on-disk dry sliding wear (which is primarily controlled by intra-lamellar features such as carbide dissolution and carbon deficiency, Section 3.4.1) and consistently with the previous PCA results (Fig. 24). The abrasive grits employed in the rubber wheel test are indeed much larger than the surface asperities coming in contact under dry sliding conditions. When they are pressed against the coating surface, they can stress many lamellae at the same time and cause the detachment of the most weakly bonded ones. This phenomenon therefore occurs more frequently in coatings obtained from the coarse feedstock powder (W2-series) on account of their poorer inter-lamellar bonding, previously inferred from porosity (Section 3.2), modulus and fracture toughness (Section 3.3) measurements.

4. Conclusions

The systematic investigations performed in this study, including the characterisation of the tribological properties of HVOF- and HVOF-sprayed WC–10Co4Cr coatings under sliding and abrasive wear conditions, and the related statistical analyses of the resulting data lead to the following conclusions:

- Different from other types of carbon-deficient sintered and crushed feedstock powders [22], the one used in this study exhibits a carbon

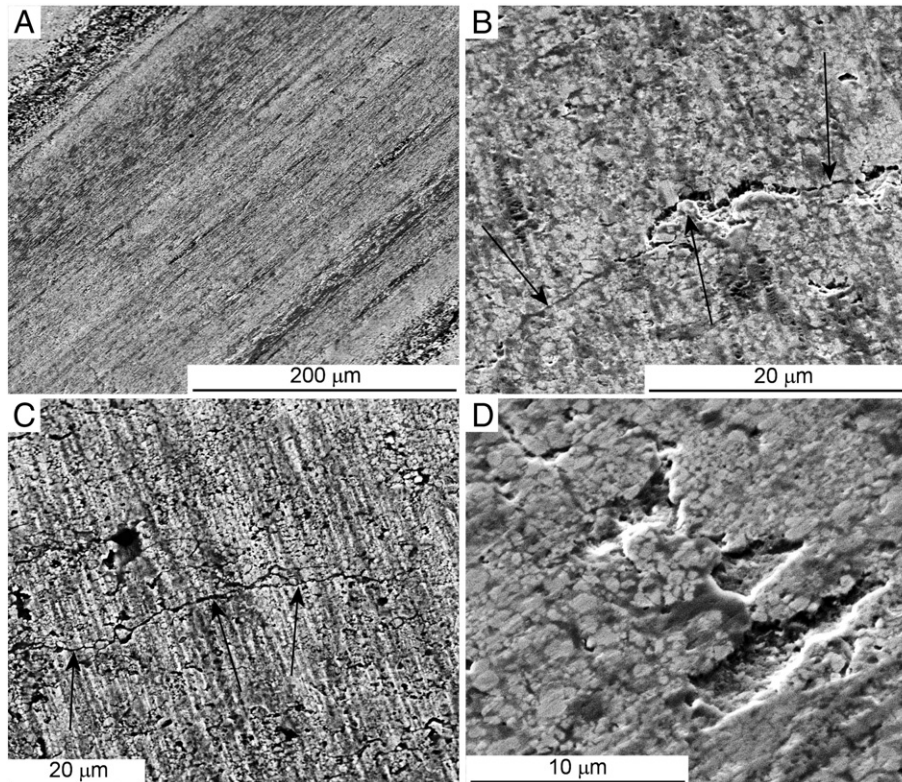


Fig. 20. SEM micrographs of wear scars after ball-on-disk tests at 400 °C: overview of sample P1W1 (A), detail of cracks (arrows) on samples P1W1 (B) and P2W1 (C) and detail of adhesive delaminations on sample P1W1 (D).

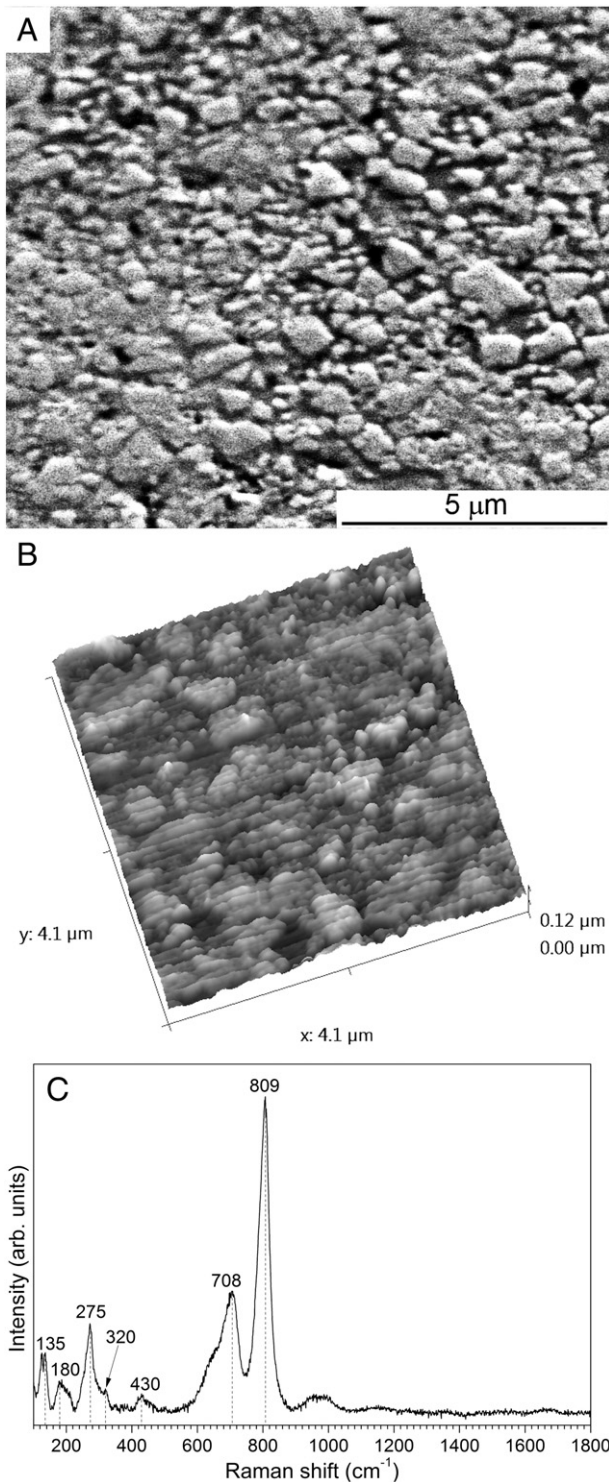


Fig. 21. SEM micrograph (A), AFM map (B) and Raman spectrum (C) acquired on the surface of sample P1W1 after ball-on-disk testing at 400 °C, outside the wear scar. All Raman peaks labelled in panel (C) are ascribed to WO₃ according to [62].

content above the nominal value. This leads to the formation of (Co,Cr,W)₇C₃ which exists as large grains in the powder and is found in the HVOF coatings as well, due to low carbon loss in this process. It is not found in the HVOF coatings due to more intensive metallurgical reactions and higher carbon loss.

- All HVOF- and HVAF spray processes used in this study are capable of producing dense WC–10Co4Cr coatings. The former cause higher carbon loss, and thus lower WC content in the coatings. In all deposition

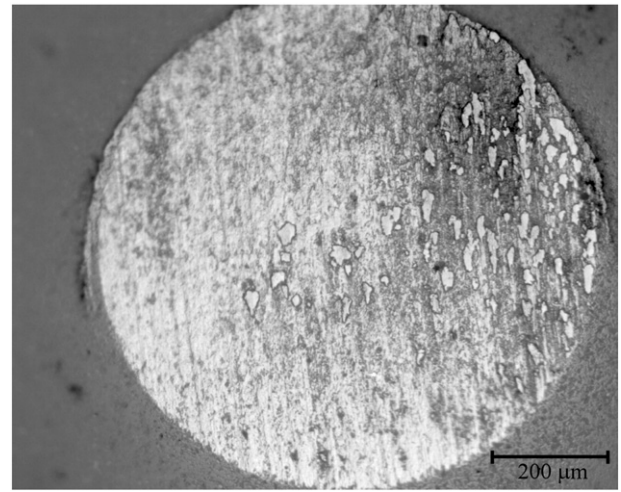


Fig. 22. Optical micrograph of the wear scar on the Al₂O₃ counterpart after ball-on-disk testing against sample P4W2 at 400 °C.

processes, the finer feedstock powder produces denser and harder coatings, with higher indentation fracture toughness and higher elastic modulus than the coarse one.

- At room temperature, the dry sliding wear behaviour of WC–10Co4Cr coatings is dominated by two concurrent mechanisms: ductile flow, which causes the formation of “wavy” lips with protruding WC grains, and brittle fracture, which causes direct detachment of small portions of material from the coating surface.

The relative incidence of the two mechanisms is mainly controlled by intra-lamellar features, such as decarburisation. This is probably related to the small size of the contacting asperities, which matches with the intra-lamellar length scale. HVOF-sprayed coatings obtained from fine feedstock powders, being somewhat more decarburised, therefore suffer slightly higher wear loss due to the increased incidence of brittle fracture phenomena.

In all cases, anyway, both the coatings and the alumina counterpart are in a mild wear regime. Friction coefficients are roughly around 0.5, with no adhesion between the mating bodies. The nanometric size of the wear debris is also consistent with very mild wear process.

- At 400 °C, WC grains at the coating surface are oxidised to WO₃. More severe abrasive grooving takes place, and adhesion to the counterpart also occurs. Wear rates increase by one order of magnitude and the friction coefficient is roughly doubled to ≈ 1.
- At 400 °C, tensile stresses due to thermal expansion mismatch with the substrate can sometimes cause complete failure of the coating

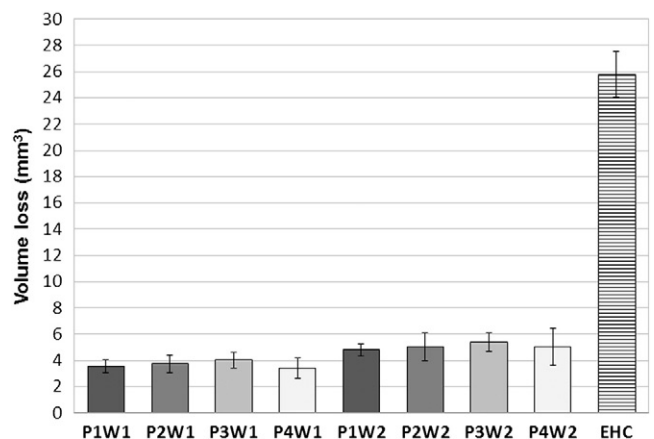


Fig. 23. Volume losses of all samples after dry sand–rubber wheel testing.

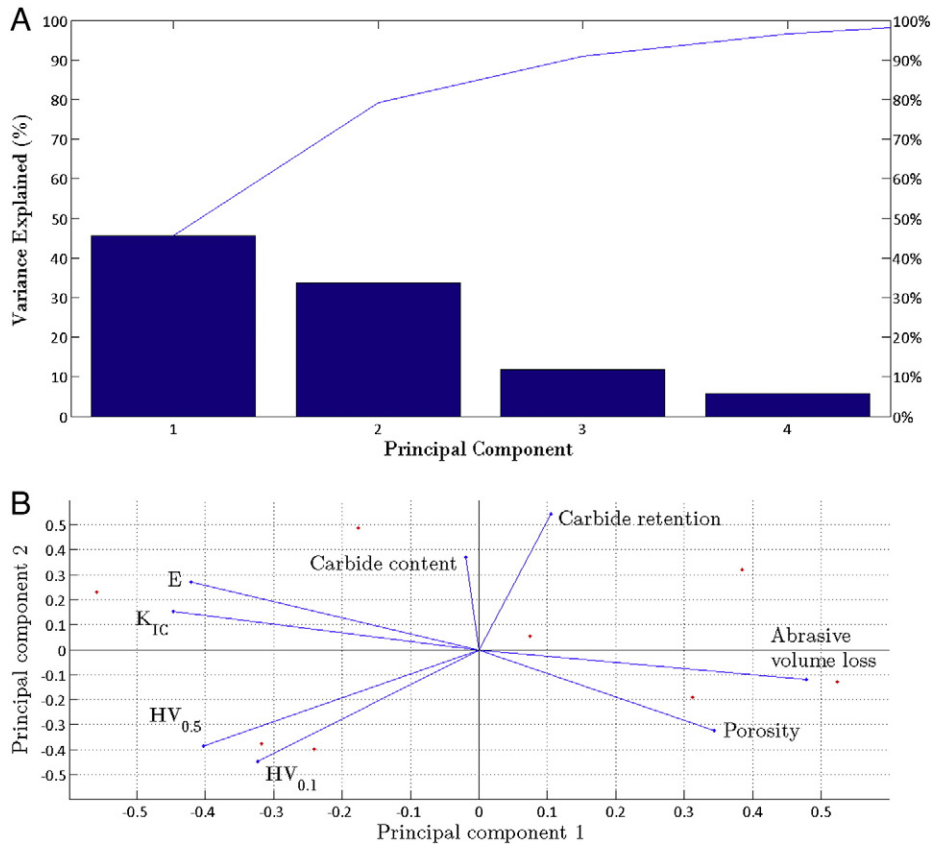


Fig. 24. Results of principal component analysis for abrasive wear testing: (A) Pareto chart, and (B) plot of the variable coefficients (vectors) and of the observation scores (dots) along the 1st and 2nd principal components.

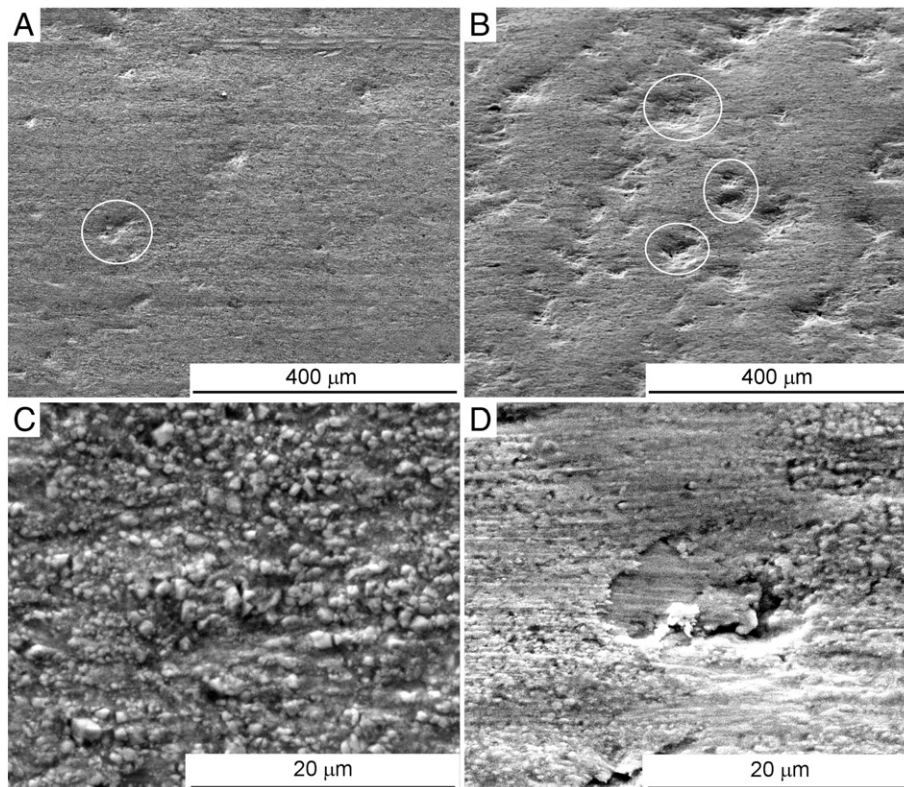


Fig. 25. SEM micrographs of wear scars produced by dry sand–rubber wheel testing: overviews of samples P1W1 (A) and P4W2 (B) and details of samples P1W1 (C) and P3W1 (D). The circles indicate lamellar detachments.

by brittle cracking, if they are coupled to pre-existing tensile residual stresses after deposition. Spraying processes capable of inducing lower residual stresses are therefore favoured in this case, as they can restrain or prevent this phenomenon. In any case, cracking across the wear scar is observed even in non-failed samples, indicating a dangerously high tensile stress level in all coatings.

- The dry particle abrasion behaviour is mainly controlled by inter-lamellar cohesion. Coatings obtained from coarse feedstock powders have weaker cohesion, which is also witnessed by lower elastic modulus, lower indentation fracture toughness and higher porosity compared to the corresponding coatings obtained from fine feedstock powders, and therefore suffer more severe abrasive wear due to the increased incidence of inter-lamellar detachment phenomena.
- It is concluded that both HVOF- and HVAF-spraying processes are able to produce coatings with satisfactory tribological properties, which are deemed to be suitable for industrial applications. The selection of the deposition process and of the feedstock powder should be made depending on the specific application, as distinct tribological conditions may probe different coating properties, as shown above.
- At room temperature, under both abrasive and sliding wear conditions, all of the tested WC–10Co4Cr coatings are more wear resistant than reference electroplated hard chromium.

Acknowledgements

Many thanks to Dr. Benno Gries, Dr. Stefan Zimmermann and Dr. Olav Norheim (H.C. Starck GmbH, Laufenburg, Germany) for providing the feedstock powders and the JP5000-HVOF sprayed coatings for this research, and to Mr. Moreno Ghiaroni (Galvanica Nobili s.r.l., Marano Sul Panaro (MO), Italy) for providing hard chromium electroplated samples.

The authors are grateful to Ing. Chiara Venturelli (Expert System Solutions s.r.l., Modena, Italy) for optical dilatometer tests and to Dr. Mauro Zapparoli (University of Modena and Reggio Emilia) for assistance with TEM observations. In addition, the authors express thanks to Mr. Roberto Puschmann for spraying samples at Fraunhofer IWS and to Mr. Andrea Milanti (Tampere University of Technology, Tampere, Finland) for XRD measurements.

References

- [1] M. Li, P.D. Christofides, *Chem. Eng. Sci.* 60 (2005) 3649–3669.
- [2] J.R. Davis (Ed.), *Handbook of Thermal Spray Technology*, ASM International, Materials Park, OH, USA, 2004.
- [3] B.D. Sartwell, K.O. Legg, J. Zimmerman, M. Reynolds, A. Drennan, J. Gribble, J. Magno, R. Mason, A. Kaltenhauser, Validation of HVOF Thermal Spray Coatings as a Replacement for Hard Chrome Plating on Hydraulic/Pneumatic Actuators, Naval Research Laboratory Final Report, 27-07-20062006.
- [4] K.O. Legg, M. Graham, P. Chang, F. Rastagar, A. Gonzales, B. Sartwell, *Surf. Coat. Technol.* 81 (1996) 99–105.
- [5] G. Montavon, A. Vardelle, N. Krishnan, P. Ulloa, S. Costil, H. Liao, in: B.R. Marple, M.M. Hyland, Y.-C. Lau, R.S. Lima, J. Voyer (Eds.), *Building on 100 Years of Success: Proceedings of the International Thermal Spray Conference 2006*, ASM International, Materials Park, OH, USA, 2006.
- [6] U.S. Department of Labor, Occupational Safety and Health Administration, Hexavalent Chromium, Report 3373-102009. (Available on-line at: <https://www.osha.gov/Publications/OSHA-3373-hexavalent-chromium.pdf>).
- [7] Off. J. Eur. Union 56 (L108) (2013) 1–5.
- [8] R. Schwetzke, H. Kreye, *J. Therm. Spray Technol.* 8 (3) (1999) 433–439.
- [9] H.M. Hawthorne, B. Arsenaull, J.P. Immarigeon, J.G. Legoux, V.R. Parameswaran, *Wear* 225–229 (1999) 825–834.
- [10] C. Bartuli, T. Valente, F. Cipri, E. Bemporad, M. Tului, *J. Therm. Spray Technol.* 14 (2) (2005) 187–195.
- [11] Q. Wang, S. Zhang, Y. Cheng, J. Xiang, X. Zhao, G. Yang, *Surf. Coat. Technol.* 218 (2013) 127–136.
- [12] L.-M. Berger, *Coatings by thermal spray*, in: V. Sarin (ed-in-chief), D. Mari, L. Llanes (vol. eds.), *Comprehensive Hard Materials – Vol. 1: Hardmetals*, Elsevier, Amsterdam, The Netherlands, 2014, p.471–506.
- [13] A. Wank, A. Schwenk, B. Wielage, T. Grund, E. Friesen, H. Pokhmurska, *Materialwiss. Werkst.* 38 (2) (2007) 144–148 (in German).
- [14] S. Kamnis, S. Gu, T.J. Lu, C. Chen, *Comput. Mater. Sci.* 43 (2008) 1172–1182.
- [15] J. Berget, T. Rogne, E. Bardal, *Surf. Coat. Technol.* 201 (2007) 7619–7625.
- [16] D.A. Stewart, P.H. Shipway, D.G. McCartney, *Wear* 225–229 (Part 2) (1999) 789–798.
- [17] P.H. Shipway, D.G. McCartney, T. Sudaprasert, *Wear* 259 (7–12) (2005) 820–827.
- [18] S. Usmani, S. Sampath, D.L. Houck, D. Lee, *Tribol. Trans.* 40 (3) (1997) 470–478.
- [19] C. Verdon, A. Karimi, J.-L. Martin, *Mater. Sci. Eng. A234–236* (1997) 731–734.
- [20] L.-M. Berger, R. Puschmann, J. Spatzier, S. Matthews, *Therm. Spray Bull.* 6 (1) (2013) 16–20.
- [21] L.-M. Berger, P. Vuoristo, T. Mäntylä, W. Kunert, W. Lengauer, P. Ettmayer, in: C.C. Berndt (Ed.), *Thermal Spray: Practical Solutions for Engineering Problems – Proceedings of the 9th National Thermal Spray Conference*, ASM International, Materials Park, OH, USA, 1996, pp. 97–106.
- [22] L.-M. Berger, P. Ettmayer, P. Vuoristo, T. Mäntylä, W. Kunert, *J. Therm. Spray Technol.* 10 (2) (2001) 311–325.
- [23] K. Frisk, A. Markström, *Int. J. Mater. Res.* 99 (3) (2008) 287–293.
- [24] B. Gries, S. Zimmermann, Corrosion behaviour of HVOF sprayed carbide coatings, in: *Proceedings of the 9th HVOF Kolloquium, Gemeinschaft Thermisches Spritzen eV, Unterschleißheim, Germany, 2012*, pp. 71–78.
- [25] M. Magnani, P.H. Suegama, N. Espallargas, S. Dosta, C.S. Fugivara, J.M. Guilemany, A.V. Benedetti, *Surf. Coat. Technol.* 202 (2008) 4746–4757.
- [26] Q. Wang, Z. Chen, L. Li, G. Yang, *Surf. Coat. Technol.* 206 (2012) 2233–2241.
- [27] S. Houdková, M. Kašparová, F. Zahálka, *Proceedings of the 19th International Conference on Metallurgy and Materials*, 18–20 May 2010, Czech Republic, 2010 (Available on-line at: http://www.metal2014.com/files/proceedings/metal_10/lists/papers/34.pdf).
- [28] E. Bergonzini, G. Bolelli, B. Bonferroni, L. Lusvardi, T. Varis, U. Kanerva, T. Suhonen, J. Oksanen, O. Söderberg, S.-P. Hannula, in: B.R. Marple, A. Agarwal, M.M. Hyland, Y.-C. Lau, C.-J. Li, R.S. Lima, A. McDonald (Eds.), *Thermal Spray 2011: Proceedings of the International Thermal Spray Conference*, DVS-Verlag, Düsseldorf, Germany, 2011, pp. 23–34.
- [29] G. Bolelli, I. Hulka, H. Koivuluoto, L. Lusvardi, A. Milanti, K. Niemi, P. Vuoristo, *Surf. Coat. Technol.* 247 (2014) 74–89.
- [30] Y. Qiao, Y.R. Liu, T.E. Fischer, *J. Therm. Spray Technol.* 10 (1) (2001) 118–125.
- [31] J.A. Picas, M. Punset, M.T. Baile, E. Martín, A. Forn, *Surf. Interface Anal.* 43 (2011) 1346–1353.
- [32] I. Hulka, V.-A. Šerban, K. Niemi, P. Vuoristo, J. Wolf, *Diffus. Defect Data B Solid State Phenom.* 188 (2012) 422–427.
- [33] L. Jacobs, M.M. Hyland, M. De Bonte, *J. Therm. Spray Technol.* 8 (1) (1999) 125–132.
- [34] L. Jacobs, M.M. Hyland, M. De Bonte, *J. Therm. Spray Technol.* 7 (2) (1998) 213–218.
- [35] L.-M. Berger, M. Woydt, S. Saaro, *Wear* 266 (2009) 406–416.
- [36] Q. Yang, T. Senda, A. Hirose, *Surf. Coat. Technol.* 200 (2006) 4208–4212.
- [37] M. Abramoff, P. Magalhães, S. Ram, *Biophotonics Int.* 11 (7) (2004) 36–42.
- [38] M.M. Lima, C. Godoy, P.J. Modenesi, J.C. Avelar-Batista, A. Davison, A. Matthews, *Surf. Coat. Technol.* 177–178 (2004) 489–496.
- [39] K. Niihara, R. Morena, D.P.H. Hasselman, *J. Mater. Sci. Lett.* 1 (1982) 13–16.
- [40] L.-M. Berger, D. Schneider, M. Barbosa, R. Puschmann, *Therm. Spray Bull.* 5 (1) (2012) 56–64.
- [41] L.-M. Berger, D. Schneider, T. Großer, in: B.R. Marple, M.M. Hyland, Y.-C. Lau, C.-J. Li, R.S. Lima, G. Montavon (Eds.), *Global Coating Solutions – Proceedings of the 2007 International Thermal Spray Conference*, ASM International, Materials Park, OH, USA, 2007, pp. 916–921 (CD).
- [42] S. Thiele, K. Sempf, K. Jaenicke-Roessler, L.-M. Berger, J. Spatzier, *J. Therm. Spray Technol.* 20 (1–2) (2011) 358–365.
- [43] www.matweb.com (last accessed 17/02/2014).
- [44] P. Niranatlumpong, C. Sukhonket, J. Nakgoenthong, *Wear* 302 (2013) 878–881.
- [45] A.C. Vermeulen, *Mater. Sci. Forum* 490–491 (2005) 131–136.
- [46] A.C. Vermeulen, D. Götz, *Mater. Sci. Forum* 524–525 (2006) 793–800.
- [47] U. Welzel, J. Ligot, P. Lamparter, A.C. Vermeulen, E.J. Mittemeijer, *J. Appl. Crystallogr.* 38 (2005) 1–29.
- [48] B. Eigenmann, *Materialwiss. Werkst.* 27 (9) (1996) 426–437 (in German).
- [49] A. Portinha, V. Teixeira, J. Carneiro, M.G. Beghi, C.E. Bottani, N. Franco, R. Vassen, D. Stoefer, A.D. Sequeira, *Surf. Coat. Technol.* 188–189 (2004) 120–128.
- [50] J. Zackrisson, B. Jansson, G.S. Upadhyaya, H.-O. Andrén, *Int. J. Refract. Met. Hard Mater.* 16 (4–6) (1998) 417–422.
- [51] G. Bolelli, L.-M. Berger, M. Bonetti, L. Lusvardi, *Wear* 309 (2014) 96–111.
- [52] P. Vuoristo, in: D. Cameron (Ed.), *Comprehensive Materials Processing*, vol. 4, Elsevier, Amsterdam, The Netherlands, 2014, pp. 229–276.
- [53] T. Varis, T. Suhonen, A. Ghabchi, A. Valarezo, S. Sampath, X. Liu, S.-P. Hannula, *J. Therm. Spray Technol.* 23 (6) (2014) 1009–1018.
- [54] P. Stecher, F. Benesovsky, H. Nowotny, *Pulvermetallurgie* 12 (2) (1964) 89–95 (in German).
- [55] M.M. Lima, C. Godoy, J.C. Avelar-Batista, P.J. Modenesi, *Mater. Sci. Eng. A* 357 (1–2) (2003) 337–345.
- [56] S. Houdková, M. Kašparová, *Eng. Fract. Mech.* 110 (2013) 468–476.
- [57] M. Xie, S. Zhang, M. Li, *Appl. Surf. Sci.* 273 (2013) 799–805.
- [58] Q. Wang, Z. Chen, L. Li, G. Yang, *Surf. Coat. Technol.* 206 (8–9) (2012) 2233–2241.
- [59] J. Nohava, B. Bonferroni, G. Bolelli, L. Lusvardi, *Surf. Coat. Technol.* 205 (4) (2010) 1127–1131.
- [60] K. Kato, K. Adachi, *Wear* 253 (2002) 1097–1104.
- [61] L.-M. Berger, M. Woydt, S. Saaro, in: R. Suchentrunck (Ed.), *Reib-/Gleitverschleiß von thermisch gespritzten Hartmetallschichten*, Jahrbuch Oberflächentechnik, vol. 63, Eugen G. Leuze Verlag, Bad Saulgau, 2007, pp. 242–267.
- [62] J.E. Herrera, D.E. Resasco, *J. Phys. Chem. B* 107 (2003) 3738–3746.
- [63] H. Mohrbacher, B. Blanplain, J.-P. Celis, J.R. Roos, *J. Mater. Sci. Lett.* 14 (1995) 279–281.
- [64] J.E. Maslar, W.S. Hurst, W.J. Bowers Jr., J.H. Hendricks, M.I. Aquino, I. Levin, *Appl. Surf. Sci.* 180 (1–2) (2001) 102–118.

- [65] J. Yang, H. Cheng, W.N. Martens, R.L. Frost, *J. Raman Spectrosc.* 42 (2011) 1069–1074.
- [66] Sh. Khameneh Asl, M. Heydarzadeh Sohi, K. Hokamotoa, M. Uemura, *Wear* 260 (2006) 1203–1208.
- [67] Q. Wang, L. Li, G. Yang, X. Zhao, Z. Ding, *Surf. Coat. Technol.* 206 (2012) 4000–4010.
- [68] Y.C. Tsui, T.W. Clyne, *Thin Solid Films* 306 (1997) 23–33.
- [69] G. Bolelli, V. Cannillo, L. Lusvardi, R. Rosa, A. Valarezo, W.B. Choi, R. Dey, C. Weyant, S. Sampath, *Surf. Coat. Technol.* 206 (8–9) (2012) 2585–2601.
- [70] L.E. Toth, *Transition Metal Carbides and Nitrides*, Academic Press, New York and London, 1971. 176–184.
- [71] A.S. Kurlov, A.I. Gusev, *Tungsten Carbides. Structure, Properties and Application in Hardmetals* Springer Series in Materials Science, vol. 184, Springer, Heidelberg, Germany, 2013. 34–36.
- [72] S.N. Basu, V.K. Sarin, *Mater. Sci. Eng. A* 209 (1996) 206–212.
- [73] Y. Liu, Y. Qiao, J. He, E. Lavernia, T.E. Fischer, *Metall. Mater. Trans. A* 33 (2002) 159–164.
- [74] J.K.N. Murthy, B. Venkataraman, *Surf. Coat. Technol.* 200 (2006) 2642–2652.
- [75] P. Suresh Babu, B. Basu, G. Sundararajan, *Wear* 268 (11–12) (2010) 1387–1399.